

AN ABSTRACT OF THE THESIS OF

ANDREAS SCHMID for the degree of MASTER of SCIENCE in
PHYSICS presented June 5th 1986

Title: COLLECTIVE ELECTRON BEHAVIOR IN ELECTRON-HOLE
SUPERLATTICES

Abstract approved: *Redacted for Privacy*

Unusual plasmas consisting of periodic layers of spatially separated electrons and holes can be fabricated by molecular beam epitaxial techniques. These materials are referred to as type II superlattices but also include the class of doping superlattices called n-i-p-i lattices. Layer thickness can be controlled to the order of 10 - 100 times atomic dimensions so that quantum mechanical effects result in quasi one-dimensional electronic subbands in the direction perpendicular to the layers. Inter and intra-layer coulomb interactions create plasma modes with acoustic dispersion which may be observed by inelastic light scattering (Raman effect). Plasmon dispersion relations for some typical structures are calculated taking into account the finite thickness and finite separation of the plasma layers.

Collective Electron Behavior in Electron-Hole
Superlattices

by

Andreas Schmid

A Thesis

submitted to

Oregon State University

in partial fulfillment of

the requirements for the

degree of

Master of Science

Completed June 5th 1986

Commencement June 1987

APPROVED:

Redacted for Privacy

Professor of Physics, in charge of major

Redacted for Privacy

Chairman of the Department of Physics

Redacted for Privacy

Dean of Graduate School

Date thesis is presented: June 5 1986

TABLE OF CONTENTS

	Page
(1) Introduction	1
(a) Superlattices: Description	1
(b) Superlattices: Fabrication	2
(c) Superlattices: Electronic Structure	3
(d) Superlattices: Doping and Band Bending	10
(e) N - I - P - I Structures	12
(f) Strained Layer Superlattices	15
(g) Superlattices: Optical Properties	16
(h) Superlattices: The present Calculation	18
(2) Raman Scattering Crosssection	21
(a) Open Diagrams	21
(b) Closed Diagrams	25
(c) The Theoretical Model of Electron-Hole Superlattices Used in the Present Calculation	29
(d) Formalism	30
(e) Calculation	35
(3) Results	45
(a) Plasmon Dispersion in a N-I-P-I Structure	45
(b) Plasmon Dispersion in a Type II Hetero- structure	48

(c) Dependence of Plasmon Energies on the Thickness of the Carrier-Confining Layers	49
(d) Remarks About Limitations of the Present Calculation	60
References	62
Appendix	64

LIST OF FIGURES

- Fig. 1. A schematic molecular beam epitaxy system. 4
- Fig. 2. Schematic real space energy diagram of a type I superlattice. 6
- Fig. 3. Schematic energy diagram of a semiconducting InAs - GaSb superlattice. 8
- Fig. 4. Schematic energy diagram of a semimetallic InAs - GaSb superlattice. 8
- Fig. 5. Band edge energies with respect to the vacuum level and lattice constants versus alloy composition in $\text{In}_{1-x}\text{Ga}_x\text{As}$ and $\text{GaSb}_{1-y}\text{As}_y$. 9
- Fig. 6. Calculated subband energies and widths for electrons and heavy and light holes as a function of the period thickness in InAs - GaSb superlattice. 9
- Fig. 7. Calculated energy levels, density distribution of electrons and the self-consistent potential in the case of modulation doping. 11
- Fig. 8. Schematic real space energy diagram of a N-I-P-I superlattice. 13
- Fig. 9. Schematic real space energy diagram of a "hetero N-I-P-I" superlattice. 13

Fig. 10. Schematic diagram of the electronic wavefunctions used in the present calculation.	38
Fig. 11. Layer sequence of a heterojunction doping superlattice.	46
Fig. 12. Backscattering geometry.	46
Fig. 13. Plasmon dispersion in a N-I-P-I structure.	52
Fig. 14. Plasmon dispersion in a type II hetero-structure.	55
Fig. 15. The phase velocities of the acoustic plasmons in a N-I-P-I superlattice as a function of the thickness of the carrier confining layers.	57
Fig. 16. Dependence of the plasmon energies in a N-I-P-I superlattice on the ratio of the thickness of the confining layers.	59

LIST OF TABLES

Table 1a.	Plasmon dispersion in a hetero n-i-p-i crystal.	50
Table 1b.	Plasmon dispersion in a hetero n-i-p-i crystal.	51
Table 2a.	Plasmon dispersion in a type II heterostructure.	53
Table 2b.	Plasmon dispersion in a type II heterostructure, neglecting finite layer thickness.	54
Table 3.	Plasmon phase velocities as a function of the thicknesses of the carrier confining layers.	56
Table 4.	Plasmon energies as a function of the ratio of the layer thicknesses of the carrier confining layers.	58

Collective Electron Behavior in Electron-Hole Superlattices

1) Introduction

(a) Superlattices: Description

Generally speaking a superlattice is a three dimensional lattice on which a one dimensional periodic modulation is imposed. Superlattices can be made of widely varying materials, e.g. metals, superconductors, magnetic materials and semiconductors. The present work investigates some fundamental effects in semiconducting superlattices produced by electron correlation between plasma confined in the layers of the superlattice.

Superlattices are artificially produced structures of periodically deposited thin (50-400Å) layers of material. The layers are smaller in thickness than the electron mean free path so that one dimensional quantum effects may be expected. The superlattice layers can differ in chemical composition over a wide range to produce electronic energy that is different in each layer. The periodic alternation in electronic structures gives rise to a larger periodicity superimposed on the atomic periodicity of the host materials which in turn gives rise

to "mini- Brillouin zones" in wavevector space and to one-dimensional energy subbands. In addition to these states, a variety of other effects which have bulk material counterparts such as excitons, donor levels, acceptor levels or phonons can be observed, but each of these is substantially altered by the superlattice environment.

(b) Superlattices: Fabrication

To fabricate superlattices, one grows thin crystalline films of alternating dissimilar materials on top of a substrate, where the substrate will determine the crystallinity and the orientation of the grown layers. This process is called heteroepitaxy. A number of heteroepitaxial growth techniques have been developed. Among the most widely used techniques are liquid-phase epitaxy, chemical-vapor deposition, and molecular beam epitaxy (MBE). In liquid-phase epitaxy the layers are grown by cooling a heated metallic solution, saturated with the components needed to grow the layers, while that solution is in contact with the substrate. In chemical-vapor deposition the epitaxial layers are grown from a heated stream of gaseous elements or compounds that react on the surface of the substrate (1).

The development of MBE has made it possible to produce high quality superlattices that are "exact" on an atomic scale, i.e., the boundaries between layers are atomically sharp, and the thickness and compositional profile of the layers are controlled to great accuracy (2). In MBE (figure 1) deposition takes place under ultrahigh vacuum conditions with precise control features. The substrate is held at a suitable temperature, and is alternately or simultaneously exposed to several molecular beams. Each of the beams is controlled by the process control computer through a mass spectrometer, which monitors the flux rates of the beams, and the shutters and heaters of each source. The apparatus also contains a high energy electron diffractometer to check the smoothness of the surface, which is the most important criterion for evaluating the success of the superlattice. Before the superlattice is started, the substrate is Argon-ion bombarded to eliminate contaminants like Carbon and Oxygen. The residual contamination of the surface can be monitored by an Auger analyzer.

(c) Superlattices: Electronic Structure

Two major types of semiconductor superlattices are

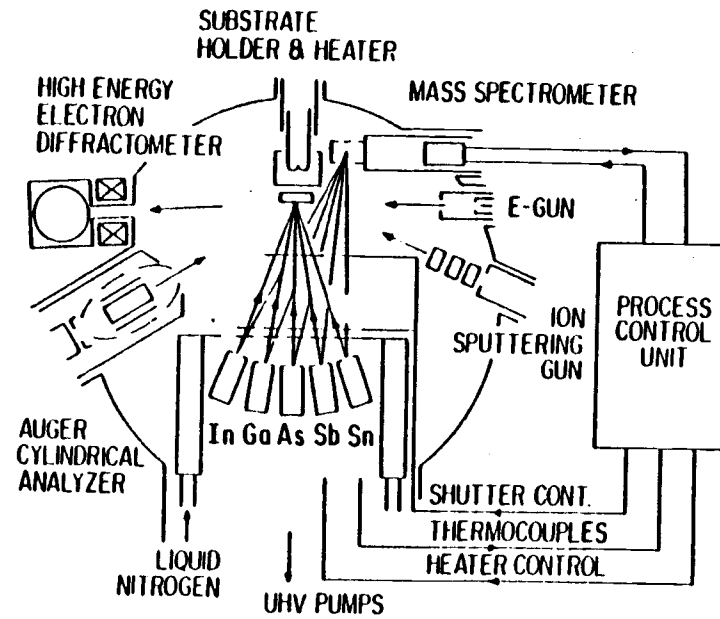


Fig. 1. A schematic, molecular beam epitaxy system for the deposition of In Ga As - GaSb As superlattice.

distinguished by their electronic structure; in particular by the relative position of the band edges in the two host materials. They are broadly referred to as type I and type II.

In a type I superlattice, typically made from GaAs - $\text{Al}_x\text{Ga}_{1-x}\text{As}$, the bandgap of one host semiconductor (GaAs) is entirely enclosed in the bandgap of the other host semiconductor (figure 2). This will cause electrons and holes that are released in any layer to diffuse into the "square wells" in the GaAs layers, which are separated by the $\text{Al}_x\text{Ga}_{1-x}\text{As}$ potential barriers. The one dimensional potential well quantizes the electronic motion along the superlattice direction, and splits the GaAs conduction band into a series of subbands. In the plane perpendicular to the superlattice direction, the electrons remain "free". Under suitable conditions, such a superlattice may be modeled as a periodic system of two-dimensional electron gas. Much attention has recently been focused on type I superlattices, because it is possible to selectively dope the $\text{Al}_x\text{Ga}_{1-x}\text{As}$ layers, and thereby achieve a system, in which most carriers are confined to the GaAs layers, while the ionized donors remain in the $\text{Al}_x\text{Ga}_{1-x}\text{As}$ layers. This will give rise to a very high carrier mobility, due to the elimination of scattering from donor ions.

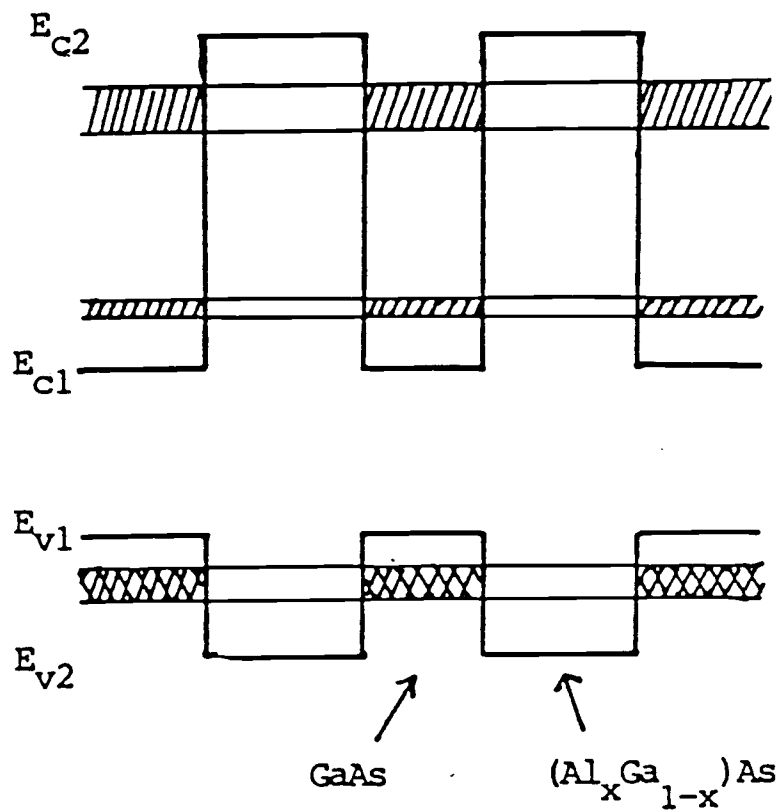


Fig. 2. Schematic real space energy diagram of a type I superlattice. The shaded areas indicate electron and hole subbands.

The type II superlattice system is typified by the InAs-GaSb system (or more generally $Ga_xIn_{1-x}As - GaAs_ySb_{1-y}$). Unlike the type I system, here the band edges are such that the band edge discontinuities across an interface have the same sign for valence band edges and conduction band edges (figure 3 and 4).

This kind of periodic potential can be looked at as a series of one-dimensional potential wells for electrons in the (Ga)InAs layers, and a series of one-dimensional potential wells for holes in the Ga(As)Sb layers. Thus one can have the unique situation of electrons and holes separating into different spacial regions.

By choosing the right alloy compositions, one can achieve a situation where the conduction band minimum in (Ga)InAs is below the valence band maximum of Ga(As)Sb. For small layer thickness, the subband system of the electrons in the (Ga)InAs layer does not overlap with the hole subband system in the Ga(As)Sb layer. (This is because the one-dimensional potential well states get "pushed up" for small well width.) For larger thicknesses the lowest electron subbands can come down below the upper valence subbands (figures 5 and 6). As a consequence, electrons from the upper valence subbands will occupy the lowest conduction subbands, even at zero temperature. This means that such a superlattice will behave like a

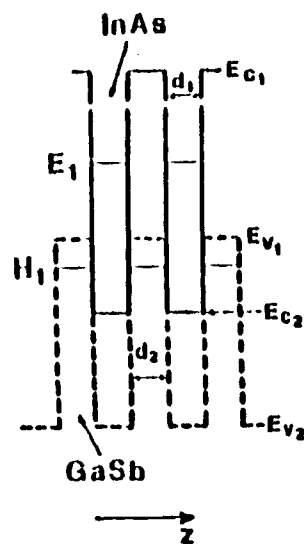


Fig. 3.

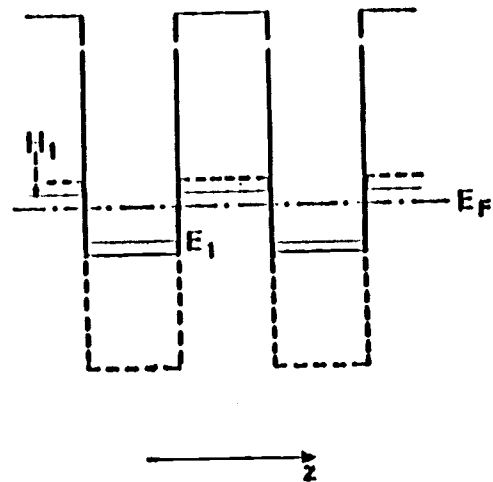


Fig. 4.

Schematic energy diagrams of semiconducting (fig. 3) and semimetallic (fig. 4) InAs - GaSb superlattices. E_{C1} (E_{C2}) and E_{V1} (E_{V2}) are the conduction and valence band edges of GaSb (InAs), respectively, along the z direction perpendicular to the layers. E_1 and H_1 indicate electron and hole subbands.

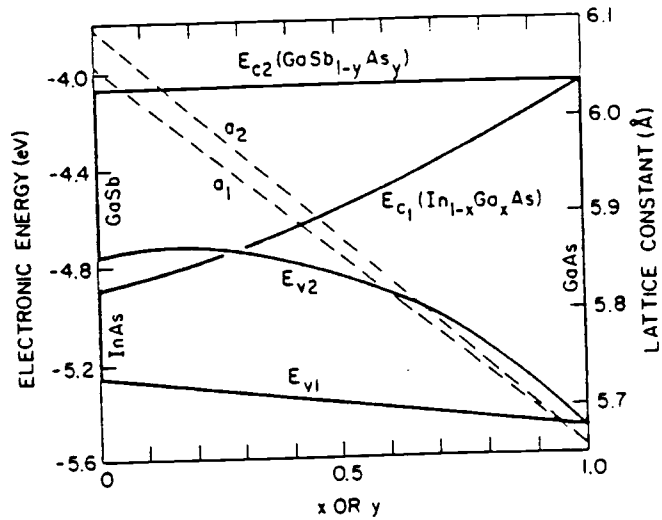


Fig. 5. Bandedge energies with respect to vacuum level and lattice constants versus alloy composition in $\text{In}_{1-x}\text{Ga}_x\text{As} - \text{GaSb}_{1-y}\text{As}_y$ (from L. L. Chang and L. Esaki).

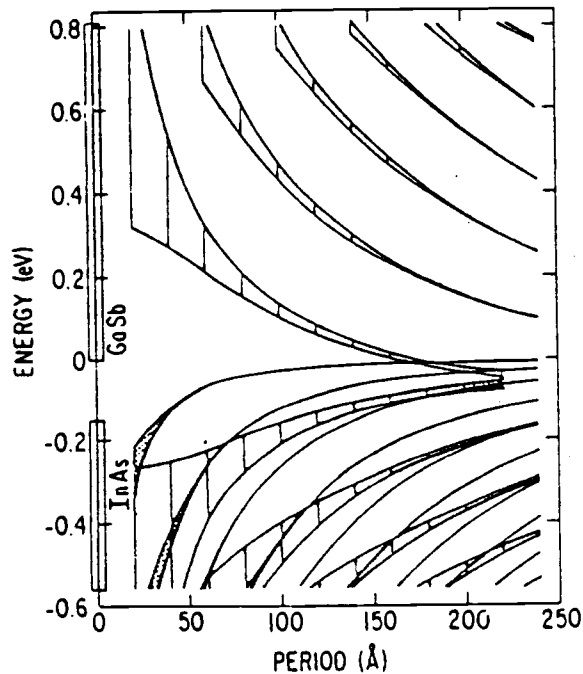


Fig. 6. Calculated subband energies and widths for electrons and heavy and light holes as a function of the period thickness in InAs - GaSb superlattice. The cross-over of the electron and heavy hole subbands at 170\AA indicates the semiconductor - semi-metal transition (from L. L. Chang and L. Esaki).

semimetal, with the two types of carriers being separated in real space rather than in momentum space (as in usual semimetals).

(d) Superlattices: Doping and Band Bending

In order to increase carrier densities, superlattices can be doped either uniformly or in specific layers only. The latter technique is called modulation doping.

A modification of the bandstructure can result from high carrier densities in doped superlattices. For example when a type I superlattice is doped (n-type or p-type), the carriers released from the impurities migrate into the GaAs potential wells, forming space charge layers there, which leaves space charge layers of the opposite sign in the AlGaAs regions due to the uniform distribution of ionized impurities. The coulomb interaction between the charges in GaAs and the ions in AlGaAs tends to restrain charge migration and concentrates the carriers close to the interfaces in a self consistent fashion (figure 7). This effect results in a modification of the potential well called band bending, because when included in the model it results in the potential wells being

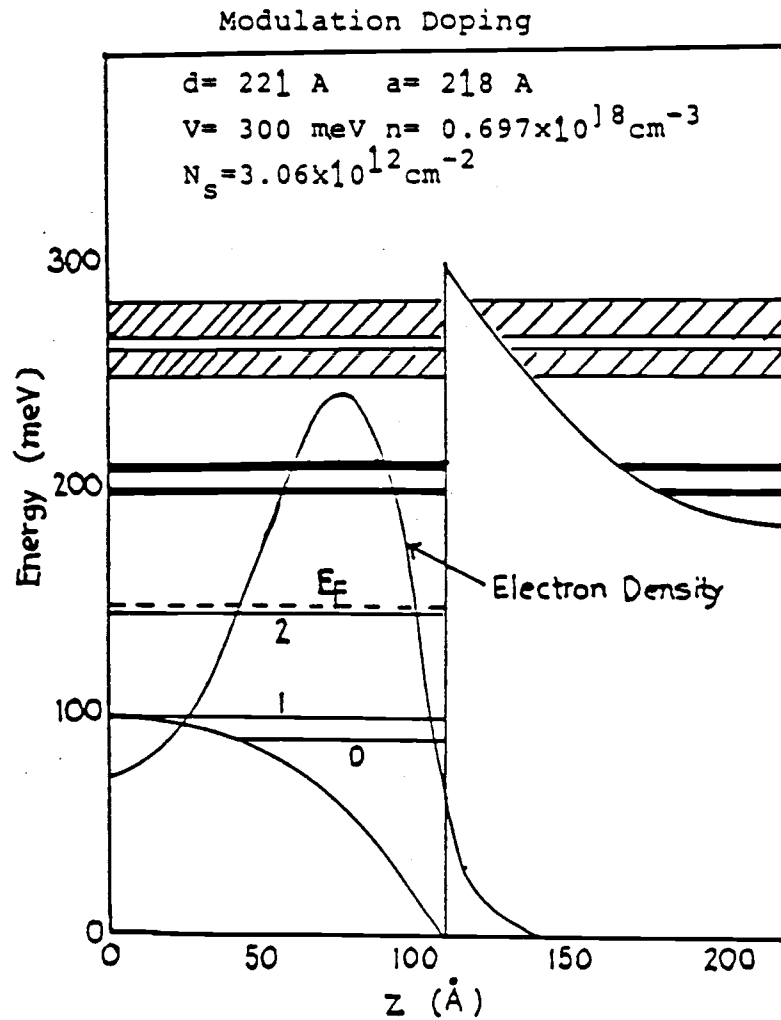


Fig. 7. Calculated energy levels, density distribution of electrons and the self-consistent potential in the case of modulation doping. The subband widths are described by hatches (from S. Mori and T. Ando).

bent (3).

In type II superlattices, bandbending can occur not only in the case of doping, but also in undoped systems where the lowest valence subband lies higher in energy than the lowest conduction subband.

(e) N - I - P - I Structures

A new kind of semiconductor superlattice which consists of ultrathin n- and p-type doped layers of a single material, possibly separated by intrinsic layers ("n-i-p-i" crystal), has recently been investigated (11). In these structures, the superlattice potential arises purely from band bending of the valence and conduction bands of the bulk material, due to the formation of space charge layers (figure 8). It is possible to modify the doping superlattice by incorporating undoped layers of a lower band gap material in the center of each doping layer, in order to confine the carriers in the undoped layers and thereby increase their mobility (figure 9). Such structures are known as "hetero - n-i-p-i" crystals.

In contrast to the above mentioned compositional superlattices, n-i-p-i structures show tunability of their electronic and optical properties over a wide range simply

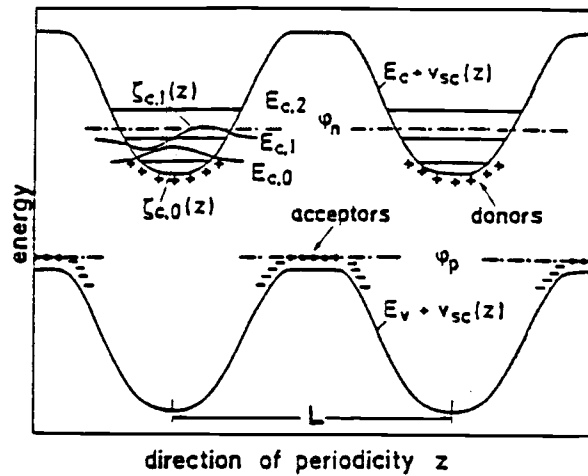


Fig. 8. Schematic real space energy diagram of a n-i-p-i crystal (from G. H. Dohler et al.).

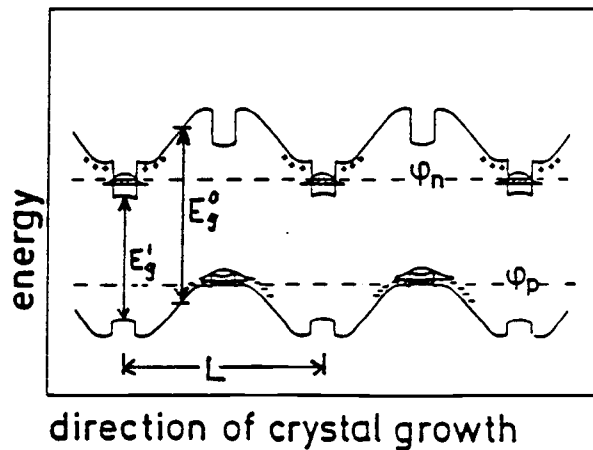


Fig. 9. Schematic energy diagram of a "hetero n-i-p-i" crystal. The doping superlattice of the crystal with bulk bandgap E_g^0 is modified by the incorporation of undoped layers of a lower bandgap material ($E_g^1 < E_g^0$). The spatial separation of the carriers from the impurity atoms enhances carrier mobility.

by photoexcitation or by injecting carriers into the p- and n-layers via selective electrodes. The tunability arises because the spatial separation between electrons and holes gives rise to a large recombination lifetime. Large deviations of the electron concentration in the n-layers and the hole concentration in the p-layers from the thermal equilibrium are metastable. The free carriers in the n- and p-layers partially compensate the fixed impurity space charge, which reduces the amplitude of the periodic space charge potential. This increases the effective band gap and modifies the subband structure (4).

An interesting feature of doping superlattices with respect to plasmon excitations is that they represent excellent candidates for the observation of acoustic plasmons and their effects on single particle absorptions. These plasmons originate from the spatially separated dynamically two-dimensional electron and hole systems which under suitable conditions exist in n-i-p-i crystals. The energy of these modes can be calculated considering only a single subband and neglecting excitonic and finite thickness effects, as discussed previously by various authors (8). In this work a discussion of plasma oscillations in a n-i-p-i crystal considering the finite thickness of the layers is included.

(f) Strained-Layer Superlattices

Although semiconductor superlattices have been grown primarily from lattice matched materials, it proved to be possible to produce superlattice structures of high crystalline quality from lattice-mismatched materials, provided that the layers are kept sufficiently thin (5,6). A key observation was that one could grow dislocation-free materials thicker by an order of magnitude than was predicted by equilibrium theories of dislocation formation (7). (For example GaAs -GaAs_{0.5}P_{0.5} superlattices with a mismatch of 1.8% can be grown with individual layer thicknesses of up to $\sim 250\text{\AA}$ without the generation of misfit dislocations (5).) In these structures, the lattice mismatch between the layers is totally accommodated by uniform strain in the layers, so that no misfit defects are generated at the interfaces. Strained-layer superlattices can thus be grown from a wide variety of alloys, forming a broad new class of semiconductor materials with electronic properties that are potentially tailorable to a variety of applications.

In order to grow strained layer superlattices with high quality layers on an inexpensive substrate with a different lattice constant, a graded buffer region can be incorporated between the substrate and the superlattice.

In the buffer region the layer stresses (due to the difference in lattice constants) drive dislocations to the edge of the sample so that the superlattice grown on top of the buffer region is free of misfit defects. Unlike lattice matched systems, the strained-layer superlattice band gaps are found to depend on layer thicknesses not only through quantum mechanical effects, but also through the strains in the layers. For example the energy subbands of carriers that are confined to one kind of layers can be shifted depending on the thickness of the other kind of layers, because the stress in the confining layers depends on the ratio of thicknesses of the two kinds of layers (5). This is not possible in lattice-matched systems. Other possible effects of layer strain are changes in the symmetry of the bulk materials. For example the heavy-hole - light-hole degeneracy at $k = 0$ may be lifted, when the crystal symmetry is changed due to stress.

(g) Superlattices: Optical Properties

Optical methods have provided considerable information about the electronic structure of the superlattice. Among the most widely used experimental

techniques are (i) far infrared absorption spectroscopy which has revealed detailed electronic subband structure and magnetic subband splitting, (ii) photoluminescence which has been used to investigate subband structure and excitonic behavior and (iii) Raman scattering (12). Raman scattering is unique among the optical experiments in that it can be used to explore many body effects that result from electron correlation between layers in the superlattice. Typical long wavelength optical experiments cannot sample behavior that results from the short wavelength periodicity of the superlattice. But Raman scattering which depends on wavevector transfer to the incident photon by the electrons can sample such behavior. Generally speaking Raman efficiencies are small, so that the light scattering intensity is not great. However, if the incident (or scattered) light frequency is almost equal to a real electronic transition the scattering intensity increases by at least an order of magnitude. This is called the resonant Raman effect and has made Raman scattering a practical experimental tool for both electronic subband structure and collective electronic effects. Indeed, tuning through the resonance can even provide additional information about the intermediate states. An additional feature of Raman scattering is that the incident and scattered light can be examined with

selected polarizations. If the incident and scattered light are of parallel polarization then the scattering intensity is proportional to the electronic density correlation function and this is the principal arrangement for investigating collective effects. On the other hand if the incident and scattered light are perpendicularly polarized then collective effects cannot be selected for observation. Yet a substantial crosssection is still observed due to spin-flip scattering in which the initial and final single electron states differ in spin. The perpendicular effect can be used to explore subband transitions simultaneously with the parallel effect examination of collective behavior. The perpendicular effect is due to spin orbit coupling of the vector potential.

(h) Superlattices: The Present Calculation

Because the plasma confining layer in the superlattice is usually of the order of 100\AA the superlattice is frequently modeled as an array of two dimensional plasmas. Using such a model it was discovered by Das Sarma and Quinn (8) that for the superlattice plasmon dispersion ω_p was proportional to $q_{||}$, the

wavevector component parallel to the superlattice layer. This is contrast to the single plasma layer which was found by Stern (9) to behave according to $\omega_p \sim \sqrt{q}$. The effect of interlayer correlation is then quite important, producing the distinctive acoustic plasmon. Raman scattering experiments indeed showed that Das Sarma and Quinn had properly characterized the type I superlattice system. However the slopes of the experimentally observed curves were smaller than predicted by the two dimensional plasma model. The calculation of Wasserman and Lee (10) indicates that the discrepancy is probably due to the neglect of plasma layer thickness which has a small but measurable effect. The method of Wasserman and Lee is applied here to the type II superlattice and the n-i-p-i superlattice. Unfortunately no experimental information is yet available on the plasma dispersion of the InAs - GaSb superlattice. In particular, the author is not aware of any Raman scattering experiments in type II superlattices. However, plasma effects have been observed in n-i-p-i structures by Raman scattering (11). Finally, since the objective of the present study relates to Raman scattering, a general approach to calculation of Raman efficiencies will be presented. It is based on the Matsubara technique for the "temperature" Green's function which calculates the photon polarization and then uses the

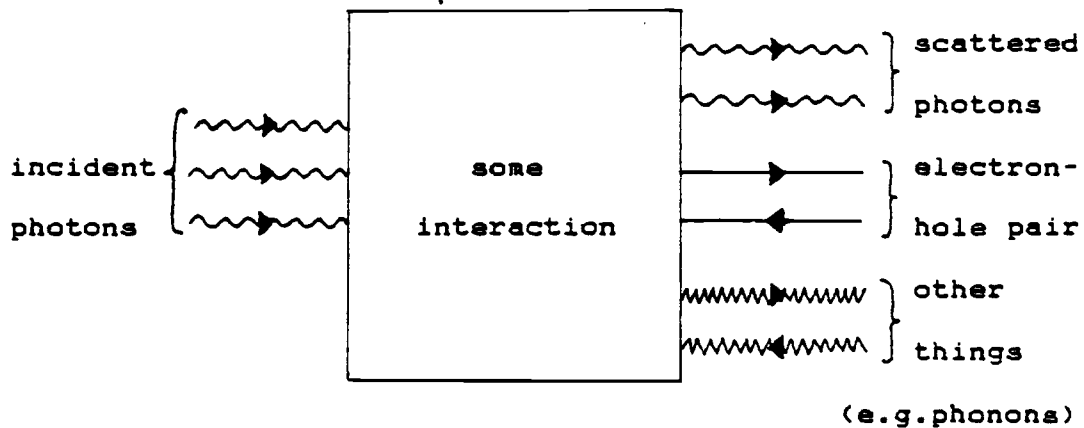
infrequently applied diagram cutting method. It exhibits, in graphical terms, the processes in which plasmon effects appear in parallel polarization Raman scattering. This approach to multiphoton processes (Raman scattering is a two-photon process) should be applicable to other classes of non-linear optical problems.

In principal the method could be used to calculate the Raman lineshape. However, the damping processes that affect the lineshape are not well understood, so that attention will be focused on the zeros of the electron density correlation function to locate the centers of the scattered peaks. The calculation as performed is limited in its applicability due to neglect of certain many-body effects which include optical phonon interactions and final state (excitonic) interactions. The latter effect is important in calculating the many-body shifted subband transitions (so called depolarization shift) but is not important for lowest plasma energies. The former effect is negligible for plasma energies far from optical phonon energies but can effect the higher energy resonantly shifted single particle transitions.

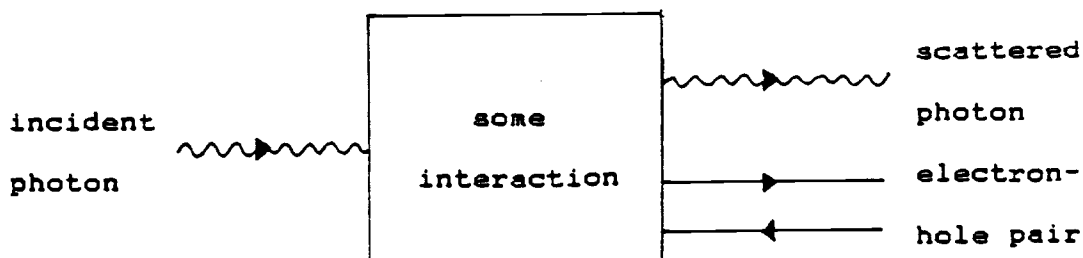
2) Raman Scattering Crosssection

(a) Open diagrams

Optical processes in an electron plasma (including absorption, emission, simple propagation, elastic and inelastic scattering....) can be drawn as open diagrams somewhat like this:




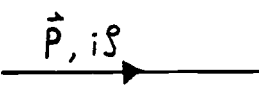
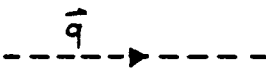
In this work, we consider only two photon processes that represent an incident and a scattered photon and a final state that consists of electron-hole pairs. The class of open diagrams is thus restricted to the following type:



Although open diagrams, which represent application of ordinary time dependent perturbation theory, can be used, we attempt a different approach which uses closed diagrams normally employed in optical absorption calculations. Optical absorption corresponds to loss of incident energy from any process, even those involving internal photons. If these lossy diagrams including internal photons are "cut" along the internal photon lines then they correspond to calculation of scattering crosssections and other non-linear transition rates. An example of such a procedure will be given in the appendix. The reason for using such a technique is that many body effects, such as electron correlations, appear and can be handled in a straightforward way. The interaction between electrons and photons and the coulomb interaction between electrons are the primary couplings in the present investigation. The technique used is a diagrammatic approach that involves a topological representation of these interactions as well as the particles that are

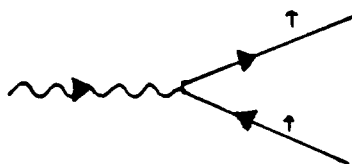
participating in the processes and shows quite explicitly the important role played by electron correlations in parallel polarization Raman scattering between single particle states.

To facilitate drawing diagrams a glossary of interactions (vertices) and particles (propagators) are needed.

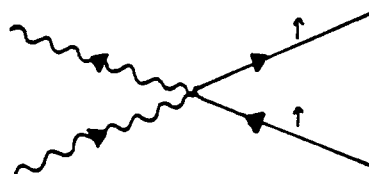
Propagators:	Symbol:	Algebraic form:
photon with wavevector \vec{k} , polarization λ and energy $i\xi$		$\frac{2\omega(\vec{k})}{(\omega(\vec{k}))^2 - (i\xi)^2}$
electron with wavevector \vec{p} and energy $i\xi$		$\frac{1}{i\xi - (E_{\vec{p}} - \mu)}$
coulomb interaction carrying wavevector \vec{q}		$\frac{e^2}{2\epsilon} \frac{e^{-q z-z' }}{q}$

Vertices:

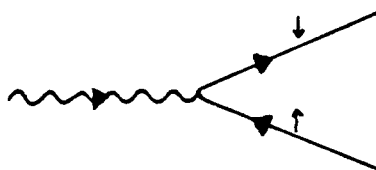
Corresponding term in the
interaction Hamiltonian:



$A \cdot p$



$A \cdot A$



$\sigma \cdot (A \times p)$

(arrows indicate spin)

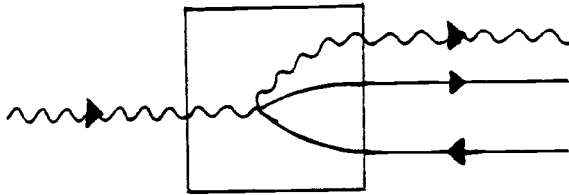
The last vertex is associated with relativistic spin-orbit coupling of the electromagnetic field to the system with spin. It can produce spin-flipping events whereas the usual terms from the non-relativistic Hamiltonian do not allow radiation fields to flip a spin unless the states have been spin-orbit split and therefore have orbitally mixed up- and down components. This last term (note the cross product) can produce the scattered radiation polarization perpendicular to the incident radiation polarization which is the signature of spin-flip scattering. Except to point out that spin-flipping reduces the allowable set of scattering diagrams to those with no electron-electron screening, we are not interested in them here precisely because they involve no plasmon related effects.

The closed diagrams considered - and the places at which they will be cut - are shown below. The rules for algebraically calculating them are given in the example in the appendix.

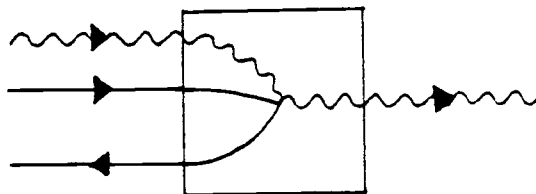
(b) Closed Diagrams

To apply the Matsubara formalism, we actually have to consider closed diagrams. These may be thought of as

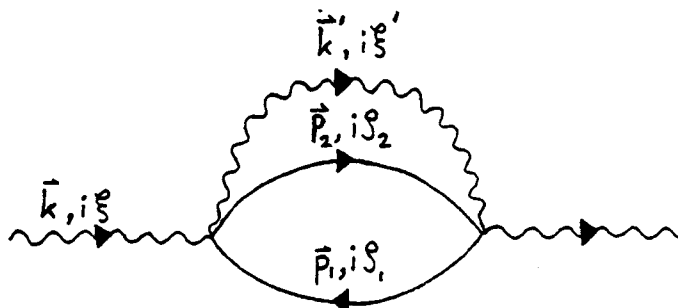
fusing two open diagrams, for example:



plus



gives



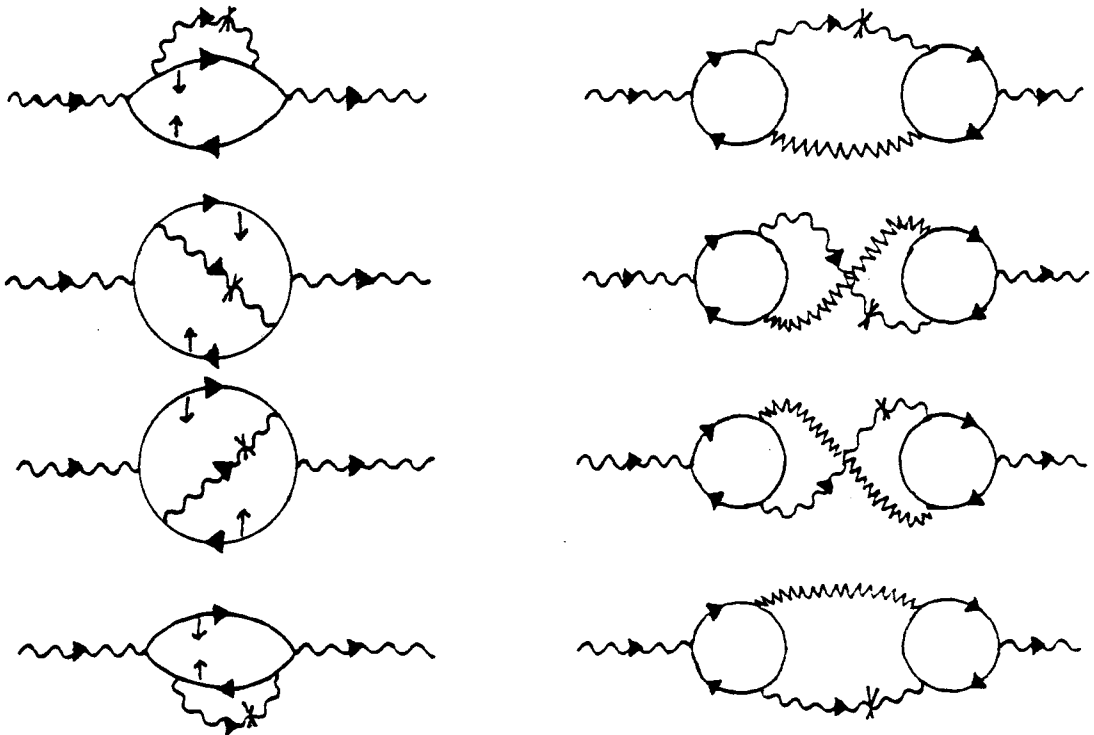
(This diagram fusion is just the Golden Rule process of squaring the matrix elements.) Using all possible vertices, we end up with the following list of closed diagrams which completely describe our problem:

Diagrams involving A·A scattering:



The diagram on the left is evaluated in detail in the appendix. The screened coulomb line ||||| appearing in the right diagram is described under (d) Formalism on page 30.

Diagrams involving A·p scattering:



Remarks:

(1) The four A-p diagrams on the left can correspond to spin-flip scattering, with the photon vertices being of the $\sigma \cdot (A \times p)$ form. The spins of single particle states are explicitly shown to emphasize the role of the spin susceptibility in these processes.

(2) The more common "classical" argument for lowest order magnetic fluctuation scattering crosssection can be seen to arise if the photons at each incoming and outgoing vertex are "collapsed" to a single two-photon vertex (16).

(3) Resonant enhancement arises from diagrams like the four A p diagrams on the right where the incident or scattered photon is connected to a virtual electron-hole pair.

(c) The Theoretical Model of Electron-Hole Superlattices
Used in the Present Calculation

As mentioned in the previous chapter, the relative positions of valence- and conduction band edges of GaSb and InAs in a multilayer superlattice system gives rise to a potential which can be modeled as a periodic system of square well potentials, confining the electrons in the InAs layers and the holes in the GaSb layers (see figure 3 and figure 4).

When the carrier densities are not too high, so that band-bending effects can be neglected, this square well model is a reasonable approximation. Furthermore, when the layer thicknesses are sufficiently large, so that the energies of the lowest subbands are low compared to the barrier heights, penetration of wavefunctions into adjacent layers can be neglected. In the present calculation the electronic wavefunctions will therefore be approximated by infinite square well wavefunctions. We will also neglect the occupation of subbands higher than zeroth order, which restricts the validity of the calculation to low temperature experiments. This is not a bad approximation, since 1°K corresponds to .1meV and subband separations are usually greater than 10meV.

(d) Formalism

The dispersion relations of the collective modes of a type II superlattice are given by the zeroes of the dielectric functions. In "subband space" the equivalent condition is that the determinate of the dielectric matrix vanishes. The dielectric matrix can be extracted from the polarization, which is defined as

$$\Pi(x, x', \tau - \tau') = \langle T_{\tau} \{ \Psi^{\dagger}(x, \tau) \Psi(x, \tau) \Psi^{\dagger}(x', \tau') \Psi(x', \tau') \} \rangle \quad (2.1)$$

where the brackets mean thermodynamic ensemble average and τ is the imaginary time as employed in the Matsubara formalism. Fourier expanding

$$\Pi(x, x', \xi_n) = \frac{1}{\beta} \int_0^{\beta} d\tau \Pi(x, x', \tau - 0) e^{i\xi_n \tau} \quad (2.2)$$

where τ is analytically continued to the imaginary axis with $-\beta < \tau < \beta$

$$\beta = \frac{1}{k_B T}, \quad \xi_n = \frac{2n\pi}{\beta}$$

In the Random Phase Approximation $\Pi(x, x', \xi_n)$ can be expressed as the following infinite sum of Feynman diagrams:

$$\begin{aligned}
 \Pi(x, x', \xi_n) = & \text{Diagram 1} \\
 + & \text{Diagram 2} \\
 + & \text{Diagram 3} \\
 + & \text{Diagram 4} \\
 + & \dots
 \end{aligned}
 \tag{2.3}$$

The diagrams in equation (2.3) represent a series of terms in a perturbation expansion. Each diagram consists of one or more circular loops representing electron (hole) propagators. The loops are connected by dashed lines representing Coulomb interactions. The first diagram is a single loop with vertices labeled x_α and x'_α , and parameters p_α, ξ_m and $q_\alpha, \xi_m - \xi_n$. The second diagram has two loops connected by a dashed line between vertices x'_α and x_β . The third diagram has three loops connected by two dashed lines. The fourth diagram has four loops connected by three dashed lines. The labels for the vertices and parameters in each diagram correspond to the indices of the loops.

where each solid line represents an electron (hole) propagator and each dashed line represents a coulomb interaction.

Each electron (hole) propagator has the form

$$G(x, x', \xi_m) = \sum_p \frac{\phi_p(x) \phi_p^*(x')}{i\xi_m - (E_p - \mu)}
 \tag{2.4}$$

where p represents all pertinent quantum numbers for the

states (\vec{k}, ν) and

$$\rho_n = \frac{(2n+1)\pi}{\beta}, \quad n = 0, \pm 1, \pm 2, \dots \quad (\text{for fermions})$$

μ is the chemical potential and $\phi_p(x)$ are the electronic wavefunctions appropriate for the non-interacting system (the subband states described in (1.c) and (2.c)) and E_p are the corresponding eigenvalues.

To evaluate the diagram equation (2.3) it is convenient to do the sums over ρ_n first since this yields a more succinct form of the zero order polarization (the "bubbles"). The zero order polarization

$$\Pi^{(0)}(x, x', \xi) = \text{bubble diagram} \quad (2.5)$$

is written out

$$\Pi^{(0)}(x, x', \xi) = \sum_{p, q, \rho_n} \frac{\phi_p(x) \phi_p^*(x')}{i\rho_n - (E_p - \mu)} \frac{\phi_q^*(x) \phi_q(x')}{i(\rho_n - \xi) - (E_q - \mu)} \quad (2.6)$$

The sum over ρ_n is done by contour integration as described in the appendix to give

$$\Pi^{(0)}(x, x', \xi) = \sum_{p, q} \frac{f(E_p - \mu) - f(E_q - \mu)}{E_p - E_q - i\xi} \phi_p(x) \phi_p^*(x') \phi_q^*(x) \phi_q(x') \quad (2.7)$$

Substituting for simplicity

$$J_{\alpha}(x_{\alpha}) = \phi_{p_{\alpha}}(x_{\alpha}) \phi_{q_{\alpha}}^{*}(x_{\alpha}) \quad (2.8)$$

(where a Greek letter index is associated with every pair p,q) and defining

$$\tilde{\pi}_{\alpha}^{(0)} = \frac{f(E_{p_{\alpha}} - \mu) - f(E_{q_{\alpha}} - \mu)}{E_{p_{\alpha}} - E_{q_{\alpha}} - i\xi} \quad (2.9)$$

and writing the coulomb matrix elements

$$V_{\alpha\beta} = \int dx'_{\alpha} \int dx_{\beta} \phi_{p_{\alpha}}^{*}(x'_{\alpha}) \phi_{q_{\alpha}}(x'_{\alpha}) V(x'_{\alpha}, x_{\beta}) \phi_{p_{\beta}}(x_{\beta}) \phi_{q_{\beta}}^{*}(x_{\beta}) \quad (2.10)$$

we can write equation (2.3):

$$\begin{aligned} \Pi(x, x', \xi) &= \sum_{\alpha, \beta, \gamma, \dots} \left\{ J_{\alpha}(x_{\alpha}) \tilde{\pi}_{\alpha}^{(0)} J_{\alpha}^{*}(x'_{\alpha}) \right. \\ &\quad + J_{\alpha}(x_{\alpha}) \tilde{\pi}_{\alpha}^{(0)} V_{\alpha\beta} \tilde{\pi}_{\beta}^{(0)} J_{\beta}^{*}(x'_{\beta}) \\ &\quad \left. + J_{\alpha}(x_{\alpha}) \tilde{\pi}_{\alpha}^{(0)} V_{\alpha\gamma} \tilde{\pi}_{\gamma}^{(0)} V_{\gamma\beta} \tilde{\pi}_{\beta}^{(0)} J_{\beta}^{*}(x'_{\beta}) + \dots \right\} \\ &= \sum_{\alpha, \beta, \gamma, \dots} J_{\alpha}(x_{\alpha}) \tilde{\pi}_{\alpha}^{(0)} \left\{ \delta_{\alpha\beta} + V_{\alpha\beta} \tilde{\pi}_{\beta}^{(0)} \right. \\ &\quad \left. + V_{\alpha\gamma} \tilde{\pi}_{\gamma}^{(0)} V_{\gamma\beta} \tilde{\pi}_{\beta}^{(0)} + \dots \right\} J_{\beta}^{*}(x'_{\beta}) \end{aligned} \quad (2.11)$$

The sum inside the brackets can be written as the matrix

$$\begin{aligned}\chi_{\alpha\beta} &= \delta_{\alpha\beta} + V_{\alpha\beta} \tilde{\pi}_{\beta}^{(0)} + \sum_{\gamma, \delta, \dots} V_{\alpha\gamma} \tilde{\pi}_{\gamma}^{(0)} V_{\gamma\delta} \tilde{\pi}_{\delta}^{(0)} + \dots \\ &= \delta_{\alpha\beta} + \sum_{\gamma} V_{\alpha\gamma} \tilde{\pi}_{\gamma}^{(0)} \chi_{\gamma\beta}\end{aligned}$$

so that

$$\sum_{\gamma} [\delta_{\alpha\gamma} - V_{\alpha\gamma} \tilde{\pi}_{\gamma}^{(0)}] \chi_{\gamma\beta} = \delta_{\alpha\beta} \quad (2.12)$$

and

$$\Pi(x, x', \xi) = \sum_{\alpha} [J_{\alpha}(x_{\alpha}) \tilde{\pi}_{\alpha}^{(0)} \chi_{\alpha\beta} J_{\beta}(x'_{\beta})]^* \quad (2.13)$$

where

$$\chi_{\tau\beta} = \sum_{\alpha} \delta_{\alpha\beta} [\delta_{\tau\alpha} - V_{\tau\alpha} \tilde{\pi}_{\alpha}^{(0)}]^{-1} \quad (2.14)$$

and

$$[\delta_{\alpha\gamma} - V_{\alpha\gamma} \tilde{\pi}_{\gamma}^{(0)}] \quad (2.15)$$

is called the dielectric matrix.

The subband separation is of the order of $\sim 100^{\circ}\text{K}$, so that for temperatures below $\sim 10^{\circ}\text{K}$ we can neglect the initial state occupancy of higher subbands. The dielectric matrix then reduces to

$$\epsilon = \begin{pmatrix} 1 - V_{oeoe} \tilde{\Pi}_{oe}^{(0)} & -V_{oeoh} \tilde{\Pi}_{oh}^{(0)} \\ -V_{ohoe} \tilde{\Pi}_{oe}^{(0)} & 1 - V_{ohoh} \tilde{\Pi}_{oh}^{(0)} \end{pmatrix} \quad (2.16)$$

where in this notation

$$V_{oeoe} = \int dx_1 \int dx_2 \phi_{oe}^*(x_1) \phi_{oe}(x_1) V(x_1, x_2) \phi_{oe}(x_2) \phi_{oe}^*(x_2)$$

$$V_{oeoh} = \int dx_1 \int dx_2 \phi_{oe}^*(x_1) \phi_{oe}(x_1) V(x_1, x_2) \phi_{oh}(x_2) \phi_{oh}^*(x_2)$$

$$V_{ohoe} = \int dx_1 \int dx_2 \phi_{oh}^*(x_1) \phi_{oh}(x_1) V(x_1, x_2) \phi_{oe}(x_2) \phi_{oe}^*(x_2)$$

$$V_{ohoh} = \int dx_1 \int dx_2 \phi_{oh}^*(x_1) \phi_{oh}(x_1) V(x_1, x_2) \phi_{oh}(x_2) \phi_{oh}^*(x_2) \quad (2.17)$$

where the subscripts refer to the subband index in the electron (e) and hole (h) layers. To find the collective modes, the zeros of the determinant of the dielectric matrix have to be found.

(e) Calculation

Electron motion parallel to the interface is considered free in the effective mass approximation. For

a given momentum parallel to the interface, the energy levels of the electrons (holes) in a square well potential of width d (width a) are quantized in the direction perpendicular to the layers. For our purpose, the envelope functions of infinite square well potentials are used[†]. This is a reasonable approximation under the assumption of small band bending. If we neglect any image potential term in the interaction, the 3-dimensional coulomb interaction is as follows:

$$V(\vec{p}-\vec{p}', z-z') = \frac{e^2}{2\epsilon} \frac{1}{(x-x')^2 + (y-y')^2 + (z-z')^2} \quad (2.18)$$

where $\vec{p} = (x, y)$.

In the present work, we are using tight binding wavefunctions, the ground states are taken to be (figure 10):

$$\text{electrons: } \phi_{0e}(\vec{p}, z) = \frac{1}{\sqrt{N}} \sqrt{\frac{2}{d}} e^{-i\vec{p}\vec{p}} \sum_m e^{-iq_z z_m} \sin \frac{\pi}{d} (z - z_m) \\ [\Theta(z - z_m + d) - \Theta(z - z_m)]$$

$$\text{holes: } \phi_{0h}(\vec{p}, z) = \frac{1}{\sqrt{N}} \sqrt{\frac{2}{a}} e^{-i\vec{p}\vec{p}} \sum_m e^{-iq_z z_m} \sin \frac{\pi}{a} (z - z_m - (d+S_1)) \\ [\Theta(z - z_m + d + S_1 + a) - \Theta(z - z_m + d + S_1)]$$

$$\text{where } z_m = m(d + S_1 + a + S_2) \quad (2.19)$$

Here d = electron layer thickness

a = hole layer thickness

S_1, S_2 are the thicknesses of the separating layers

† At this point it should be noted that self consistent calculations of the superlattice potential in n-i-p-i structures show that harmonic oscillator wavefunctions would be more appropriate (4). However, in this work we have used the square well wavefunctions also for the calculation of plasmons in n-i-p-i crystals, because we feel that this small deviation in the ground state wavefunctions will have a negligible effect on the plasma modes.

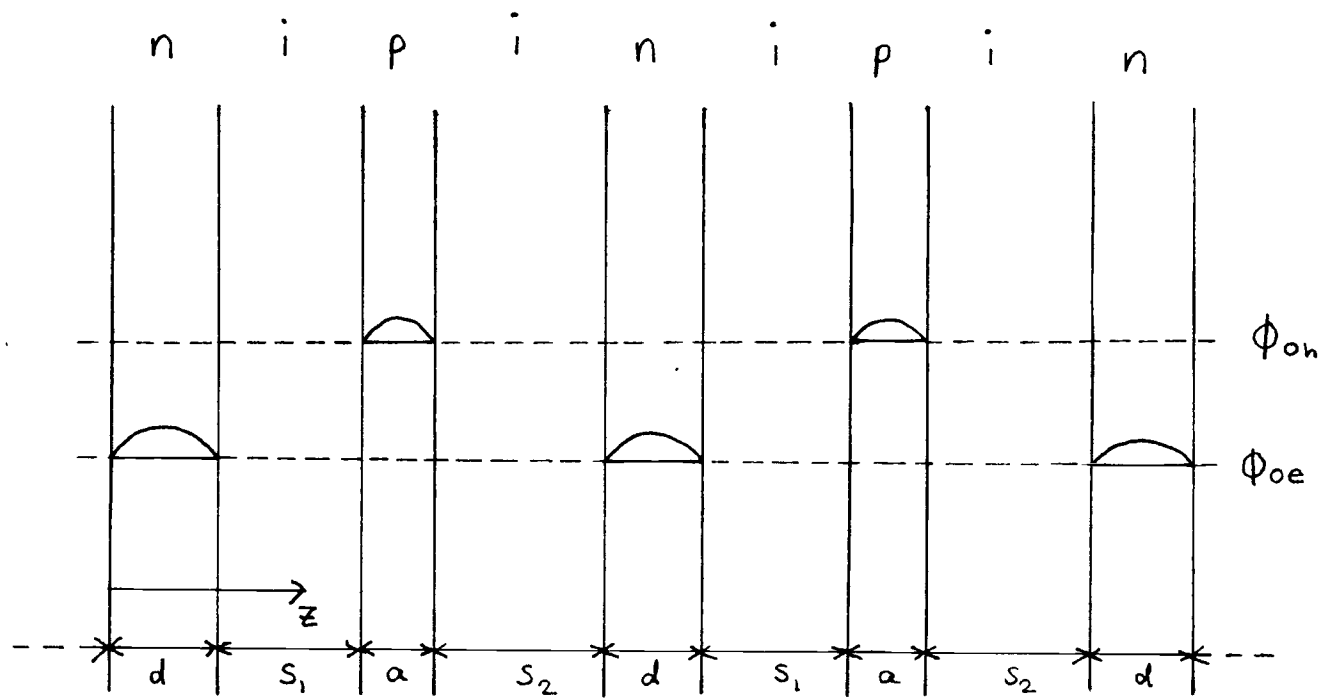


Fig. 10. Schematic diagram of the electronic wavefunctions used in the present calculation.

To calculate the matrix elements of the dielectric matrix, we use the 2-dimensional Fourier transform of the coulomb potential

$$V(q) = \frac{e^2}{2\epsilon} \frac{e^{-q|z-z'|}}{q} \quad (2.20)$$

which is equivalent to (in integral representation)

$$\frac{e^{-q|z-z'|}}{q} = \frac{1}{\pi} \int_{-\infty}^{\infty} ds \frac{e^{-is(z-z')}}{s^2 + q^2} \quad (2.21)$$

The matrix elements are then:

$$\begin{aligned} V_{oeoh} &= \frac{e^2}{2\epsilon} \frac{1}{\pi} \int_{-\infty}^{\infty} ds \frac{1}{s^2 + q^2} \\ &\int_0^d dz \frac{1}{\sqrt{N}} \sqrt{\frac{2}{d}} \sum_m e^{-isz} e^{-iq_z z_m} \sin \frac{\pi}{d} (z - z_m) \\ &\frac{1}{\sqrt{N}} \sqrt{\frac{2}{d}} \sum_m e^{+iq'_z z_m} \sin \frac{\pi}{d} (z - z_m) \\ &\int_{d+S_1}^{d+S_1+a} dz' \frac{1}{\sqrt{N}} \sqrt{\frac{2}{a}} \sum_n e^{+is z'} e^{+iq''_z z_n} \sin \frac{\pi}{a} (z' - z_n - (S_1 + d)) \\ &\frac{1}{\sqrt{N}} \sqrt{\frac{2}{a}} \sum_n e^{-iq'''_z z_n} \sin \frac{\pi}{a} (z' - z_n - (S_1 + d)) \end{aligned} \quad (2.22)$$

Substituting $\beta = z - z_m - \frac{d}{2}$, $\beta' = z' - z_n - (S_1 + d) - \frac{a}{2}$

$$\begin{aligned}
 V_{\text{oeoh}} &= \frac{e^2}{2\epsilon} \frac{1}{\pi} \int_{-\infty}^{\infty} ds \frac{1}{s^2 + q^2} \\
 &\frac{2}{Nd} \sum_m e^{-is\frac{d}{2}} e^{-i(s+q_z - q'_z)z_m} \int_{-\frac{d}{2}}^{+\frac{d}{2}} e^{-is\beta} \cos^2 \frac{\pi}{d} \beta \, d\beta \\
 &\frac{2}{Na} \sum_n e^{+is\frac{a}{2}} e^{+is(d+S_1)} e^{+i(s+q''_z - q'''_z)z_n} \int_{-\frac{a}{2}}^{+\frac{a}{2}} e^{+is\beta'} \cos^2 \frac{\pi}{a} \beta' \, d\beta'
 \end{aligned} \tag{2.23}$$

But

$$\begin{aligned}
 \int_{-\frac{d}{2}}^{+\frac{d}{2}} e^{-is\beta} \cos^2 \frac{\pi}{d} \beta \, d\beta &= \frac{d}{4} \left\{ \frac{\sin \frac{d}{2} (s - \frac{2\pi}{d})}{\frac{d}{2} (s - \frac{2\pi}{d})} + \right. \\
 &\left. \frac{\sin \frac{d}{2} (s + \frac{2\pi}{d})}{\frac{d}{2} (s + \frac{2\pi}{d})} + 2 \frac{\sin(\frac{sd}{2})}{\frac{sd}{2}} \right\}
 \end{aligned} \tag{2.24}$$

and

$$\begin{aligned}
 \sum_m e^{-i(s+q_z - q'_z)z_m} &= N \delta(s + \Delta q_z + G) \\
 \sum_n e^{i(s+q''_z - q'''_z)z_n} &= N \delta(s + \Delta q_z + G)
 \end{aligned} \tag{2.25}$$

(Δq_z is the change in optical wavevector due to scattering)

where $G = \frac{2\pi\nu}{d+S_1+a+S_2}$ and $\nu = 0, \pm 1, \pm 2, \dots$

Because of eq. (2.25)

$$s = \Delta q_z + G$$

and the phase factor

$$\begin{aligned} & e^{-is\frac{d}{2}} e^{+is\frac{a}{2}} e^{+is(d+S_1)} \\ &= e^{+i\Delta q_z(\frac{a+d}{2} + S_1)} e^{+iG(\frac{a+d}{2} + S_1)} \\ &= e^{+i\Delta q_z(\frac{a+d}{2} + S_1)} (-1)^n e^{+iG(\frac{S_1-S_2}{2})} \end{aligned} \quad (2.26)$$

Combining these results (dropping Δq_z in favor of the simpler notation q_z):

$$\begin{aligned} V_{oeoh} = V_{ohoe}^* &= \frac{e^2}{4\epsilon(d+S_1+a+S_2)} e^{+iq_z(\frac{a+d}{2} + S_1)} \\ & \sum_n (-1)^n e^{+iG(\frac{S_1-S_2}{2})} \frac{1}{(q_z+G)^2 + q^2} \left\{ \frac{\sin\frac{d}{2}(q_z+G-\frac{2\pi}{d})}{\frac{d}{2}(q_z+G-\frac{2\pi}{d})} + \right. \\ & \left. \frac{\sin\frac{d}{2}(q_z+G+\frac{2\pi}{d})}{\frac{d}{2}(q_z+G+\frac{2\pi}{d})} + \frac{2\sin\frac{d}{2}(q_z+G)}{\frac{d}{2}(q_z+G)} \right\} \\ & \left\{ \frac{\sin\frac{a}{2}(q_z+G-\frac{2\pi}{a})}{\frac{a}{2}(q_z+G-\frac{2\pi}{a})} + \frac{\sin\frac{a}{2}(q_z+G+\frac{2\pi}{a})}{\frac{a}{2}(q_z+G+\frac{2\pi}{a})} + \frac{2\sin\frac{a}{2}(q_z+G)}{\frac{a}{2}(q_z+G)} \right\} \end{aligned} \quad (2.27)$$

$$V_{oeoe} = \frac{e^2}{4\epsilon(d+S_1+a+S_2)} \sum_n \frac{1}{(q_z+G)^2 + q^2}$$

$$\left\{ \frac{\sin \frac{d}{2}(q_z+G - \frac{2\pi}{d})}{\frac{d}{2}(q_z+G - \frac{2\pi}{d})} + \frac{\sin \frac{d}{2}(q_z+G + \frac{2\pi}{d})}{\frac{d}{2}(q_z+G + \frac{2\pi}{d})} + \frac{2 \sin \frac{d}{2}(q_z+G)}{\frac{d}{2}(q_z+G)} \right\}$$

(2.28)

$$V_{onon} = \frac{e^2}{4\epsilon(d+S_1+a+S_2)} \sum_n \frac{1}{(q_z+G)^2 + q^2}$$

$$\left\{ \frac{\sin \frac{a}{2}(q_z+G - \frac{2\pi}{a})}{\frac{a}{2}(q_z+G - \frac{2\pi}{a})} + \frac{\sin \frac{a}{2}(q_z+G + \frac{2\pi}{a})}{\frac{a}{2}(q_z+G + \frac{2\pi}{a})} + \frac{2 \sin \frac{a}{2}(q_z+G)}{\frac{a}{2}(q_z+G)} \right\}$$

(2.29)

Since we are restricting the calculation to the ground states for electrons and holes, the plasma modes are given by the vanishing of the determinant of the dielectric matrix as given in eq. (2.16).

Recalling that in the superlattice tight binding approximation the electronic wavefunctions have a two-dimensional plane wave contribution parallel to the layers as well as the subband contributions perpendicular to the layers, we can write the two polarizations involved (refer to eq. (2.9))

$$\begin{aligned}\tilde{\Pi}_{oe}^{(0)} &= \sum_{\mathbf{p}} \frac{f(\mathbf{p}+\mathbf{q}, oe) - f(\mathbf{p}, oe)}{\omega - (E_{\mathbf{p}+\mathbf{q}, oe} - E_{\mathbf{p}, oe})/\hbar} \\ \tilde{\Pi}_{oh}^{(0)} &= \sum_{\mathbf{p}} \frac{f(\mathbf{p}+\mathbf{q}, oh) - f(\mathbf{p}, oh)}{\omega - (E_{\mathbf{p}+\mathbf{q}, oh} - E_{\mathbf{p}, oh})/\hbar}\end{aligned}\tag{2.30}$$

where

$$f(\mathbf{p}, \nu) = \frac{1}{e^{(E_{\mathbf{p}, \nu} - \mu)\beta} + 1}, \quad E_{\mathbf{p}, \nu} = \frac{\hbar^2 \mathbf{p}^2}{2m^*} + E_{\nu}$$

$$\text{and} \quad \mathbf{p}^2 = p_x^2 + p_y^2$$

In the small q approximation (9):

$$\tilde{\Pi}_{oe}^{(0)} = \frac{n_e}{m_e^*} \frac{q^2}{\omega^2}, \quad \tilde{\Pi}_{oh}^{(0)} = \frac{n_h}{m_h^*} \frac{q^2}{\omega^2} \quad (2.31)$$

For convenience, we rewrite these as

$$\tilde{\Pi}_{oe}^{(0)} = \frac{\Pi_{oe}}{\omega^2}, \quad \tilde{\Pi}_{oh}^{(0)} = \frac{\Pi_{oh}}{\omega^2} \quad (2.32)$$

where

$$\Pi_{oe} = \frac{n_e}{m_e^*} q^2, \quad \Pi_{oh} = \frac{n_h}{m_h^*} q^2 \quad (2.33)$$

The collective frequencies are then given by

$$\begin{aligned} \omega^2 &= \frac{1}{2} (V_{oeoe} \Pi_{oe} + V_{ohoh} \Pi_{oh}) \\ &\pm \frac{1}{2} \sqrt{(V_{oeoe} \Pi_{oe} - V_{ohoh} \Pi_{oh})^2 + 4 V_{oeoh} \Pi_{oh} V_{ohoe} \Pi_{oe}} \end{aligned} \quad (2.34)$$

3) Results

(a) Plasmon Dispersion in a N-I-P-I structure

The author is not aware of any experimental investigations of intrasubband plasmons in n-i-p-i superlattices. According to previous theoretical considerations (13), however, n-i-p-i structures represent excellent candidates for the observation of such plasmon excitations.

In this work, a calculation of the plasma modes in a superlattice similar to the hetero n-i-p-i structure described by H. Kunzel et. al. (14) is included. This superlattice configuration consists of 21 alternating n- and p-doped $\text{Al}_x\text{Ga}_{1-x}\text{As}$ regions each 110nm thick, corresponding to 10 superlattice periods. Each intentionally doped region is intersected by a stack of 13nm undoped i-GaAs sandwiched between two 11nm i- $\text{Al}_x\text{Ga}_{1-x}\text{As}$ spacer layers (figure 11). In this system, the carriers are confined in the GaAs regions. The electron and hole concentration can be varied by application of an external voltage via selective contacts.

Since the crosssection for light scattering from a two-dimensional plasma is small, it is practical to use

Fig. 11. Schematic diagram of the layer structure of the hetero n-i-p-i crystal from ref. (14).

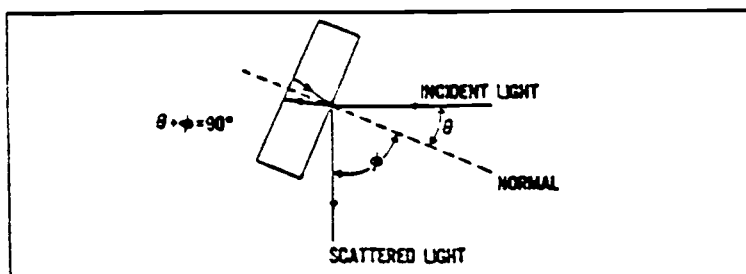
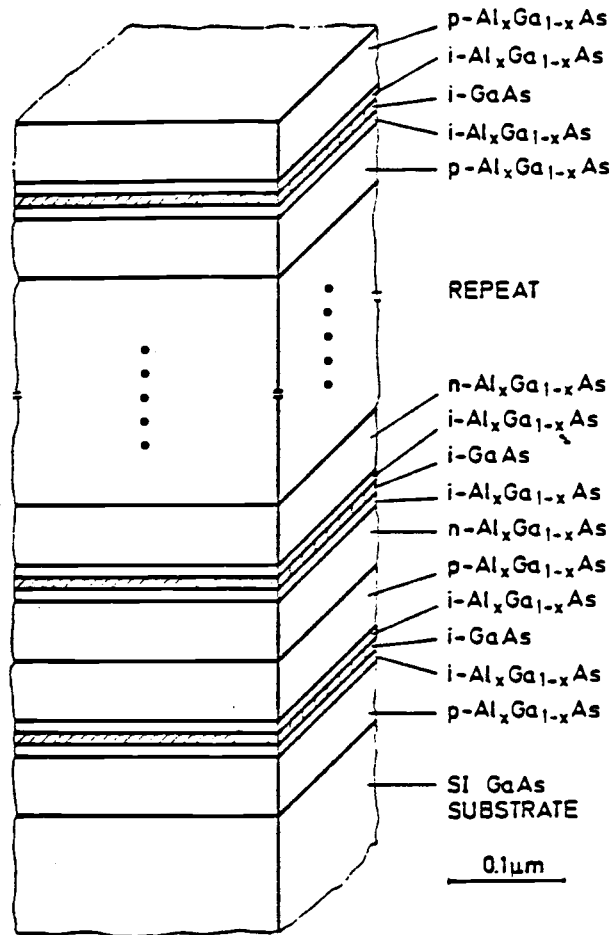


Fig. 12. Backscattering geometry.

resonance enhanced scattering. The energy of the 6471\AA Kr^+ laser line is slightly larger than the separation between the conduction band and the spin-orbit split-off valence band in GaAs, giving the desired resonance enhancement. In the backscattering geometry, which is a common configuration for this type of measurements (figure 12), the components of the wavevector are given by

$$q_{\parallel} = \frac{2\pi}{\lambda} (\sin\theta - \cos\theta) \quad (3.1)$$

and

$$q_{\perp} \cong \frac{4\pi}{\lambda} \eta \left\{ 1 - \frac{1}{4\eta^2} \right\} \quad (3.2)$$

where λ is the wavelength of the incident laser light, η is the refractive index, θ is the incident angle and ϕ is the scattered angle such that $\theta + \phi = 90^\circ$. By changing θ from 45° to 0° , q_{\parallel} can be varied from a small value up to about $1 \cdot 10^5 \text{ cm}^{-1}$. For $\eta = 3.6$, q_{\perp} has a value of about $6.6 \cdot 10^5 \text{ cm}^{-1}$ and does not depend significantly on θ . Therefore, q_{\perp} is a well defined parameter. The AlGaAs layers are transparent to the laser light. In the GaAs layers, the absorption length α^{-1} is $\sim 0.6 \mu\text{m}$, and consequently all the quantum wells should be excited. The condition $q_{\perp} L \gg 1$ holds, and therefore the electrons should respond according to the

model (see tables 1a and 1b and figure 13).

The carrier densities used in the calculation for of table 1 and figure 13 are $n = 2.2 \cdot 10^{16} \text{ m}^{-2}$ and $n = 4.7 \cdot 10^{15} \text{ m}^{-2}$.

The carrier densities n and n can be varied over a wide range by optical excitation or by application of an external voltage. Because of equations (2.33) and (2.34) the plasmon frequencies are expected be proportional to the carrier concentrations.

(b) Plasmon Dispersion in a Type II Hetero-Structure

The plasmon dispersion of a InAs-GaSb type II superlattice has been calculated previously by A. C. Tselis and J. J. Quinn (15), neglecting finite layer thickness.

Tables 2a and 2b and figure 14 show the result when finite layer thickness is included (solid lines), as well as the 0-layerthickness result from Tselis and Quinn. The result for finite layer thickness turns out to be about 13% lower than the 0-thickness result. Although this is a small difference, it is large enough that it should be detectable in an appropriate experiment.

(c) Dependence of Plasmon Energies on the Thickness of the Carrier-Confining Layers

In the small q approximation the plasmon dispersion is nearly linear. The plasmon phase velocities, which are given by the slopes of the plasmon dispersion curves, were calculated as a function of the thicknesses of the confining layers under the assumption of constant superlattice period. The value of q_{\perp} was chosen to be $q_{\perp} = 6.6 \times 10^5 \text{ cm}^{-1}$, corresponding to the 6471\AA Kr^+ laser line giving resonance enhancement in GaAs. The results are given in table 3 and figure 15.

The dependence of plasmon energies in type II superlattices on the ratio of the thicknesses of the two kinds of layers was calculated. Table 4 and figure 16 show the results for constant layerthickness $a = 100\text{\AA}$ and layerthickness b varying from 100\AA to 500\AA . The in-plane wavevector q_{\parallel} was assumed to be constant, $q_{\parallel} = 0.5/a$. The perpendicular component of the wavevector q_{\perp} varies as indicated in the figure. (Note that in the InAs - GaSb system the electron-hole plasma only exists when the layer thicknesses are greater than 170\AA).

Table 1a. Plasmon dispersion. The sample parameters correspond to the hetero n-i-p-i crystal described in ref. (14).

electron layer thickness $d = 130\text{\AA}$

hole layer thickness $a = 130\text{\AA}$

electron area density $n_e = 2.2 \cdot 10^{16} \text{ m}^{-2}$

hole area density $n_h = .47 \cdot 10^{16} \text{ m}^{-2}$

$m_c^* = .068$, $m_h^* = .544$, dielectric constant $\epsilon = 13.1$

separating layers $S1 = S2 = 970\text{\AA}$

perpendicular component of the wavevector $q_{\perp} = 6.6 \cdot 10^7 \text{ m}^{-1}$

$q_{\parallel} (10^6 \text{ m}^{-1})$	$\omega_+ (\text{meV})$	$\omega_- (\text{meV})$
0.0	0.0	0.0
2.5	3.99	0.54
5.0	7.41	1.05
7.5	10.11	1.49
10.0	12.23	1.87
12.5	13.97	2.19
15.0	15.44	2.46

Table 1b. Plasmon dispersion. The sample parameters are the same as in table 1a.

perpendicular component of the wavevector $q_{\perp} = 0$

q_{\parallel} (10^6 m^{-1})	ω_+ (meV)	ω_- (meV)
0.0		0.0
2.5	12.74	0.53
5.0	13.13	1.03
7.5	13.74	1.47
10.0	14.51	1.86
12.5	15.38	2.18
15.0	16.32	2.45

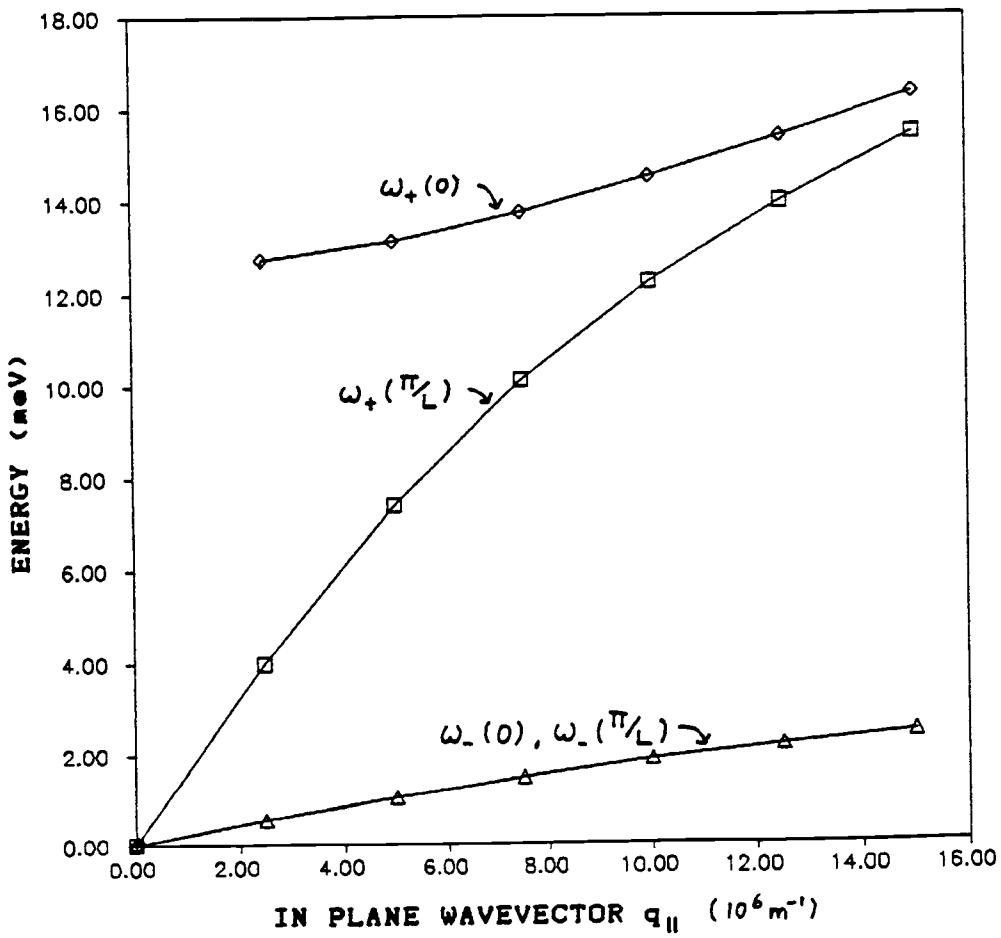


Fig. 13. Plasmon dispersion for a n-i-p-i crystal. The component of the wavevector perpendicular to the layers is indicated in the arguments of ω .

Table 2a. Plasmon dispersion. The sample parameters correspond to a type II superlattice similar to the structure described in ref (15).

electron layer thickness $d = 250\text{\AA}$

hole layer thickness $a = 300\text{\AA}$

electron area density $n_e = 4.1 \cdot 10^{15} \text{ m}^{-2}$

hole area density $n_h = 4.1 \cdot 10^{15} \text{ m}^{-2}$

$m_e = .023$, $m_h = .33$, dielectric constant $\epsilon = 15$

separating layers $S_1 = S_2 = 0$

perpendicular component of the wavevector $q_{\perp} = \pi/(a+d)$

$q_{\parallel} (10^6 \text{ m}^{-1})$	ω_+ (meV)	ω_- (meV)
0.0	0.0	0.0
6.0	2.55	0.66
12.0	5.03	1.30
18.0	7.37	1.90
24.0	9.52	2.45
30.0	11.45	2.95
36.0	13.18	3.39

Table 2b. Plasmon dispersion. The sample parameters correspond to a type II superlattice similar to the structure described in ref (15), neglecting the finite layer thickness.

electron layer thickness $d = 0$

hole layer thickness $a = 0$

separating layers $S1 = S2 = 275\text{\AA}$

electron area density $n_e = 4.1 \cdot 10^{15} \text{ m}^{-2}$

hole area density $n_h = 4.1 \cdot 10^{15} \text{ m}^{-2}$

$m_e = .023$, $m_h = .33$, dielectric constant $\epsilon = 15$

perpendicular component of the wavevector $q_{\perp} = \pi/(a+d)$

q (10^6 m^{-1})	$w+$ (meV)	$w-$ (meV)
0.0	0.0	0.0
6.0	2.83	0.75
12.0	5.59	1.48
18.0	8.22	2.17
24.0	10.66	2.81
30.0	12.90	3.41
36.0	14.94	3.94

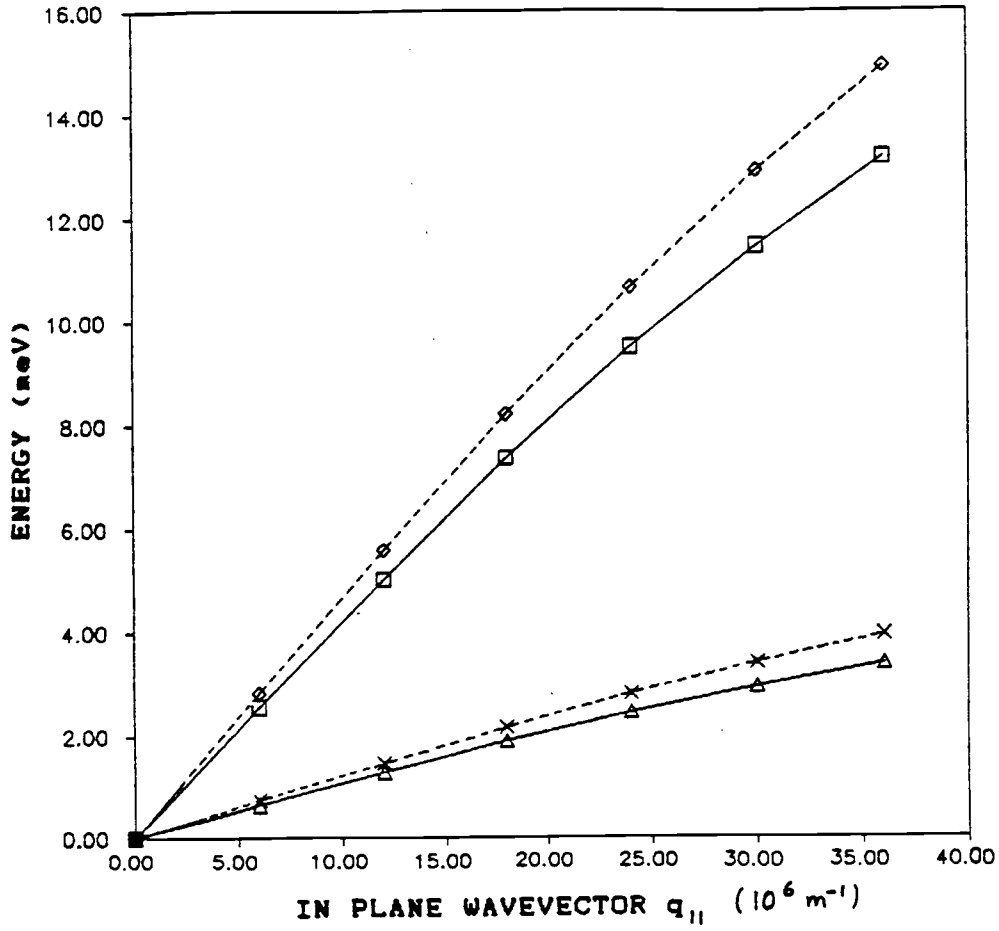


Fig. 14. Plasmon dispersion for a type II heterostructure. The dashed lines are the result when layer thickness is neglected. The solid lines are the result when layer thickness is included. The component of the wavevector perpendicular to the layers is $q_{\perp} = \pi/L$, where L is the total lattice period.

Table 3. Plasmon phase velocities as a function of the thicknesses of the carrier confining layers. The thicknesses of the confining layers are varied from 0 to half the total period. The total period is held constant.

electron area density $n_e = 4.1 \cdot 10^{15} \text{ m}^{-2}$

hole area density $n_h = 4.1 \cdot 10^{15} \text{ m}^{-2}$

$m_e^* = .068$, $m_h^* = .544$, dielectric constant $\epsilon = 13.1$

total period $L = 2200 \text{ \AA}$

perpendicular component of the wavevector $q = 6.6 \cdot 10^7 \text{ m}^{-1}$

a, d (\AA)	$v(w+)$ (10^6 m/s)	$v(w-)$ (10^6 m/s)
0	2.52	.339
100	2.50	.334
200	2.49	.330
300	2.47	.325
400	2.46	.321
500	2.44	.316
600	2.42	.311
700	2.41	.307
800	2.39	.302
900	2.37	.296
1000	2.36	.292

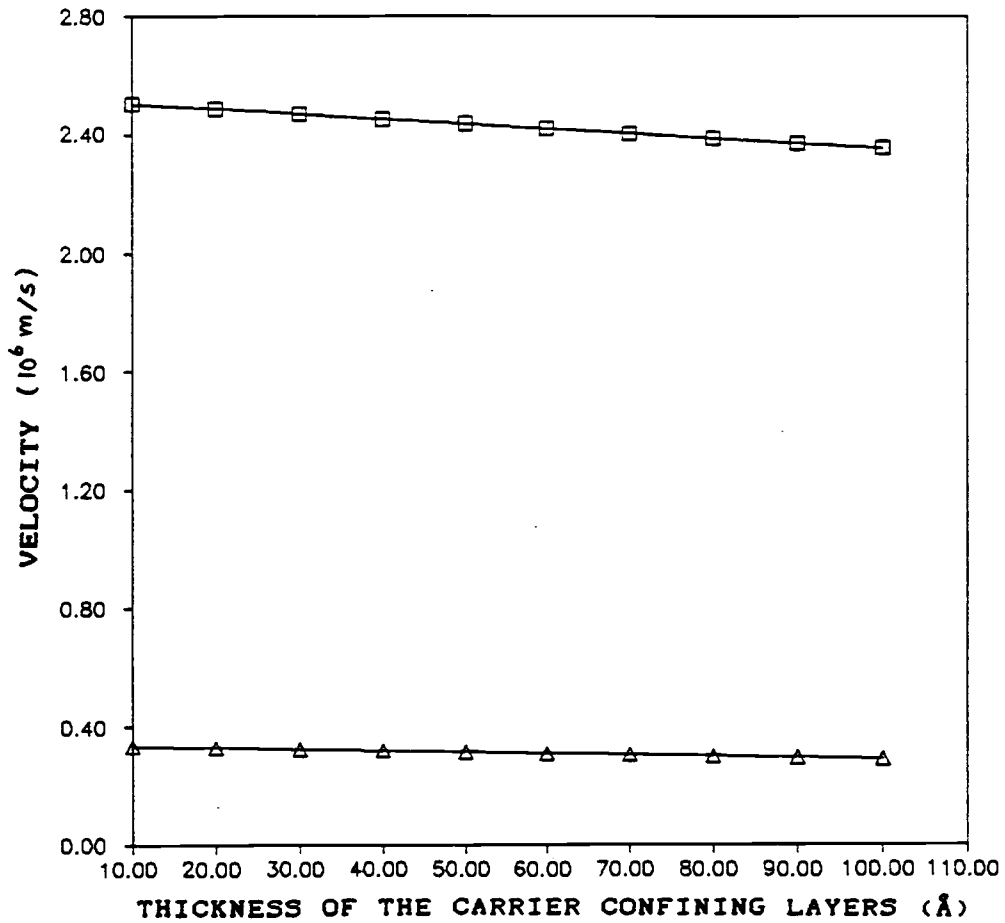


Fig. 15. The phase velocity of the acoustic plasmons in a n-i-p-i crystal as a function of the thickness of the carrier confining layers.

Table 4. Plasmon energies as a function of the ratio of the layer thicknesses b/a .

electron area density $n = 4.66 \cdot 10^{15} \text{ m}^{-2}$

hole area density $n = 2.33 \cdot 10^{15} \text{ m}^{-2}$

$m_c^* = .068$, $m_h^* = .544$, dielectric constant $\epsilon = 13.1$

hole layer thickness $a = 100\text{\AA}$

separating layers $S_1 = S_2 = 0$

perpendicular component of the wavevector

$$q = \pi/a+d \text{ or } q = 0$$

d/a	$w+(\pi/a+d)$	$w+(0)$	$w-(\pi/a+d)$	$w-(0)$
-------	---------------	---------	---------------	---------

(plasmon energies are in eV)

1	8.08	19.9	2.02	1.72
2	8.96	16.3	2.46	2.06
3	9.45	14.3	2.74	2.32
4	9.66	12.9	2.91	2.52
5	9.68	11.9	3.02	2.67

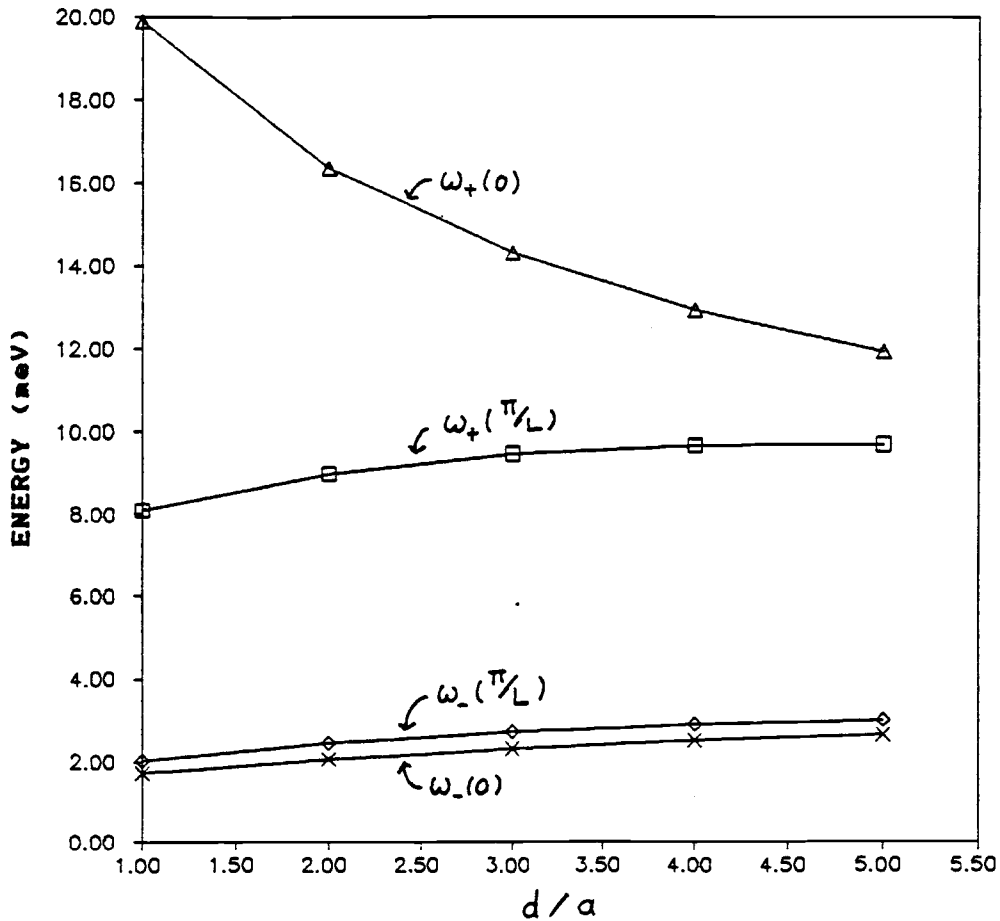


Fig. 16. The plasmon energies in a type II structure as a function of the ratio of the layer thicknesses, where the thickness of the electron layer is $a = 100\text{\AA}$, the in-plane wavevector is taken to be $q_{\parallel} = 0.5/a$ and the perpendicular component of the wavevector is as indicated in the graph.

(d) Remarks About Limitations of the Present
Calculation

This calculation has conspicuous limitations which are

- (1) only lowest subband occupation assumption,
- (2) $q \ll q_f$ in the occupied subband
- (3) no band bending in the type II configuration (note that band bending is intrinsic to the n-i-p-i structure).

For higher electron densities appropriate for the n-i-p-i structure these limitations must be addressed. In principle this is not difficult but certainly the result will not be as tractable as the present calculation.

Experimentally the most accessible plasmon information is from Raman scattering in the parallel polarization configuration where inelastic intersubband scattering is observed (11). As indicated in the Raman scattering Feynman diagrams and the text of chapter 1, even these transitions are plasmon modified. This is referred to as "resonance shifting". By including in the dielectric matrix transitions between subbands these effects can be studied. The matrices then become large and become complicated functions of the Raman frequency

shift and consequently lie beyond the objective and scope of the present study.

REFERENCES

- (1) "Epitaxial Growth", Edited by J. W. Mathews,
Academic Press (1975)
- (2) L. L. Chang, L. Esaki et al.,
J. Vac. Sci. Tech. 10 655 (1973).
- (3) S. Mori and T. Ando,
Surf. Sci. 98 101 (1980).
- (4) G. H. Dohler and P. Ruden,
Surf. Sci. 142 474 (1984).
- (5) G. C. Osbourne, R. M. Biefeld and P. L. Gourley,
Appl. Phys. Lett. 41 (2) 172 (1982).
- (6) G. C. Osbourne,
J. Appl. Phys. 53 (3) 1586 (1982).
- (7) V. Narayanamurti,
Physics Today (oct. 1984).
- (8) S. Das Sarma and J. J. Quinn,
Phys. Rev. B 25 7603 (1982).
- (9) F. Stern,
Phys. Rev. Lett. 18 546 (1967).
- (10) A. Wassermann and Y. I. Lee,
Sol. St. Comm. 54 855 (1985).
- (11) G. Fasol, P. Ruden and K. Ploog,
J. Phys. C 17 1395 (1984).

- (12) A. Pinczuk, J. M. Worlock, H. L. Stormer et al.,
Surf. Sci 98 126 (1980).
- (13) P. Ruden and G. H. Dohler,
Phys. Rev. B 27 3547 (1983).
- (14) H. Kunzel, A. Fischer, J. Knecht and K. Ploog,
Appl. Phys. A 30 73 (1983).
- (15) A. C. Tselis and J. J. Quinn,
Phys. Rev. B 29 3318 (1984).
- (16) "Scattering of Light by Crystals", W. Hayes and
R. Loudon, Wiley Interscience, N. Y. (1978).

Appendix

Appendix

The following diagram corresponds to the leading term in A.A scattering:

$$\Delta \xi = \xi - \xi'_m$$

This term is called Thomson scattering when applied to a collection of free electrons (ions).

Evaluating this diagram by algebraically inserting each propagator, we find (aside from leading constants, which shall be restored later):

$$S^{(1)} = \sum_{\vec{k}} \int d\vec{x} \int d\vec{x}' e^{-i\vec{k}\vec{x}} e^{+i\vec{k}'\vec{x}'} \sum_{s_n, \xi'_m} \sum_{\vec{p}} \frac{\phi_{\vec{p}}(\vec{x}) \phi_{\vec{p}}^*(\vec{x}')}{i s_n - (E_{\vec{p}} - \mu)}$$

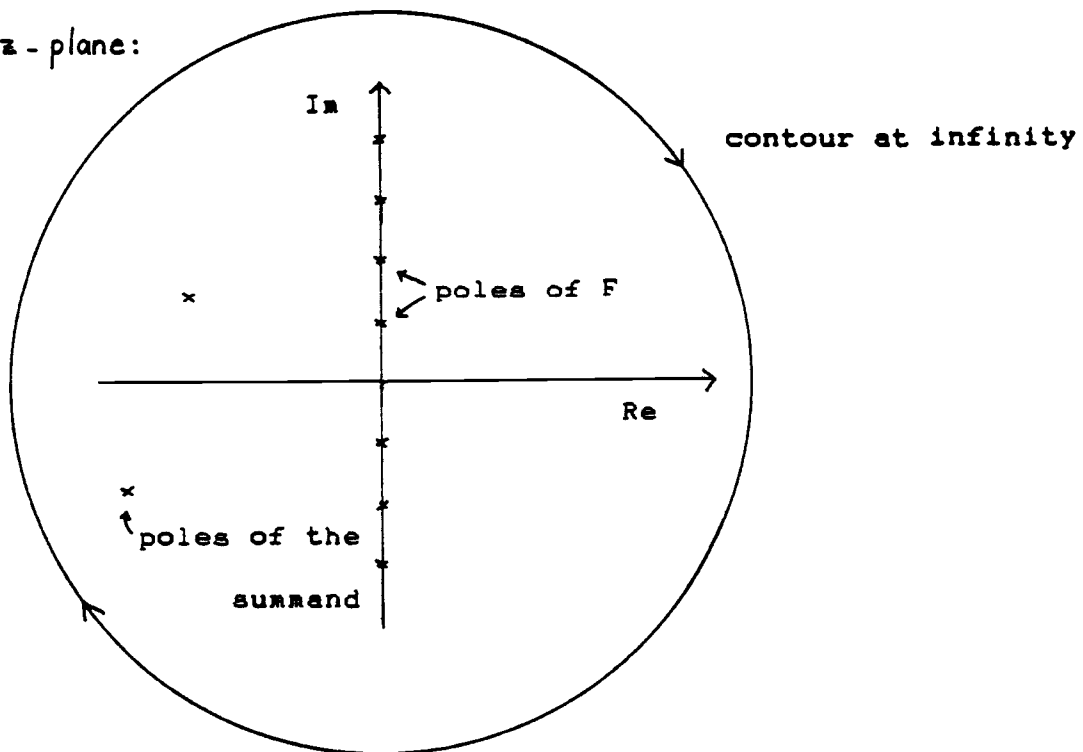
$$|\hat{\epsilon}_0 \cdot \hat{\epsilon}_s|^2 \sum_{\vec{q}} \frac{\phi_{\vec{q}}^*(\vec{x}) \phi_{\vec{q}}(\vec{x}')}{i s_n + i \Delta \xi - (E_{\vec{q}} - \mu)} \frac{2 \omega_s(\vec{k})}{\omega_s^2(\vec{k}) - (i \xi'_m)^2} e^{-i\vec{k}\vec{x}} e^{+i\vec{k}'\vec{x}'}$$

where $s_n = (2n+1)\pi/\beta$, $\xi'_m = 2n\pi/\beta$

and $\phi_{\vec{p}}(\vec{x}), \phi_{\vec{q}}(\vec{x})$ are electronic states. In a plasma they take on plane wave forms.

The sums over ξ_n and ξ'_m are typically done by contour integration. That is, the summand is analytically continued, multiplied by a function F chosen to have poles (with residues equal to one) at the values of the variable that is being summed over and finally integrated along a contour that encloses all poles. If F is chosen so that the product of F and the summand vanishes at infinity and the contour is chosen at infinity, then the contour integral, enclosing all poles, vanishes. Since the value of the contour integral is equal to the sum of the residues of all poles enclosed by the contour, evidently the sum that was to be evaluated is equal to (aside from a minus sign) the sum of the residues of the poles of the summand.

z -plane:



To carry out the sum over \mathcal{J}_n in the present case, we choose $F(z) = \frac{1}{e^{z\beta} + 1}$ (since $\mathcal{J}_n = \frac{(2n+1)\pi}{\beta}$):

$$S^{(1)} = \sum_{\vec{k}} |\hat{\epsilon}_0 \cdot \hat{\epsilon}_s|^2 \left| \int d\vec{x} e^{-i(\vec{k}-\vec{k}')\vec{x}} \phi_{\vec{p}}(\vec{x}) \phi_{\vec{q}}^*(\vec{x}) \right|^2$$

$$\sum_{\xi'_m} \frac{F(E_{\vec{q}} - \mu) - F(E_{\vec{p}} - \mu)}{E_{\vec{q}} - E_{\vec{p}} - i\Delta\xi} \left\{ \frac{1}{i\xi'_m - \omega_s(\vec{k})} - \frac{1}{i\xi'_m + \omega_s(\vec{k})} \right\}$$

also, for free electrons:

$$\int d\vec{x} e^{-i(\vec{k}-\vec{k}')\vec{x}} \phi_{\vec{p}}(\vec{x}) \phi_{\vec{q}}^*(\vec{x}) = \int d\vec{x} e^{-i(\vec{k}-\vec{k}')\vec{x}} e^{-i(\vec{p}-\vec{q})\vec{x}}$$

$$= \delta((\vec{k}-\vec{k}') + (\vec{p}-\vec{q}))$$

Next we do the sum over ξ'_m , choosing $N(z) = \frac{1}{e^{z\beta} - 1}$ (for $\xi'_m = \frac{2m\pi}{\beta}$):

$$S^{(1)} = \sum_{\vec{k}} |\hat{\epsilon}_0 \cdot \hat{\epsilon}_s|^2 \delta((\vec{k}-\vec{k}') + (\vec{p}-\vec{q})) [F(E_{\vec{q}} - \mu) - F(E_{\vec{p}} - \mu)]$$

$$\left\{ \frac{N(E_{\vec{p}} - E_{\vec{q}})}{E_{\vec{p}} - E_{\vec{q}} + i\xi - \omega_s(\vec{k})} + \frac{N(\omega_s(\vec{k}))}{E_{\vec{q}} - E_{\vec{p}} - i\xi + \omega_s(\vec{k})} \right.$$

$$\left. - \frac{N(-\omega_s(\vec{k}))}{E_{\vec{q}} - E_{\vec{p}} - i\xi - \omega_s(\vec{k})} - \frac{N(E_{\vec{p}} - E_{\vec{q}})}{E_{\vec{p}} - E_{\vec{q}} + i\xi + \omega_s(\vec{k})} \right\}$$

The second term in this result is proportional to

$$N(\omega_s(\vec{k})) = \frac{1}{e^{\hbar\omega_s\beta} - 1}$$

and can be neglected for low temperatures, when

$$\hbar\omega_s\beta \gg 1.$$

The third term and the fourth term are proportional to

$$\frac{1}{\pm \Delta E \mp (\omega_0 + \omega_s)}$$

which corresponds to processes involving two incident photons. At common incident beam intensities these processes have a negligible crosssection. Therefore we are left with

$$S^{(1)} = \sum_{\vec{k}} |\hat{\epsilon}_0 \cdot \epsilon_s|^2 \delta((\vec{k} - \vec{k}') + (\vec{p} - \vec{q})) \frac{[F(E_{\vec{q}} - \mu) - F(E_{\vec{p}} - \mu)] N(E_{\vec{p}} - E_{\vec{q}})}{E_{\vec{q}} - E_{\vec{p}} - i\xi + \omega_s(\vec{k})}$$

To cut the diagram at the indicated point, we (1)

substitute

$$i\xi \rightarrow \omega_0 + i\delta$$

$$S^{(1)} = \sum_{\vec{k}} |\hat{\epsilon}_0 \cdot \epsilon_s|^2 \delta((\vec{k} - \vec{k}') + (\vec{p} - \vec{q})) \frac{[F(E_{\vec{q}} - \mu) - F(E_{\vec{p}} - \mu)] N(E_{\vec{p}} - E_{\vec{q}})}{E_{\vec{q}} - E_{\vec{p}} - (\omega_0 + \omega_s(\vec{k})) - i\delta}$$

(2) take the limit of $\delta \rightarrow 0$

$$S^{(1)} = P - i\pi \sum_{\vec{k}} \delta((E_{\vec{q}} - E_{\vec{p}}) - (\omega_0 + \omega_s(\vec{k}))) \delta((\vec{k} - \vec{k}') + (\vec{p} - \vec{q})) \\ [F(E_{\vec{q}} - \mu) - F(E_{\vec{p}} - \mu)] N(E_{\vec{p}} - E_{\vec{q}}) |\epsilon_0 \cdot \epsilon_s|^2$$

(3) take the imaginary part only, to finally get the crosssection:

$$\sigma = \pi \sum_{\vec{k}} \delta((E_{\vec{q}} - E_{\vec{p}}) - (\omega_0 - \omega_s)) \delta((\vec{k} - \vec{k}') - (\vec{q} - \vec{p})) |\hat{\epsilon}_0 \cdot \hat{\epsilon}_s| [F(E_{\vec{q}} - \mu) - F(E_{\vec{p}} - \mu)] N(E_{\vec{p}} - E_{\vec{q}})$$

Performing the integration over \vec{k} :

$$\sum_{\vec{k}} \longrightarrow \int dk k^2 d\Omega' \frac{V}{(2\pi)^3}$$

where $k = \frac{\omega_s}{c}$ so $dk k^2 = d\omega_s \frac{\omega_s^2}{c^3}$

and we also use

$$\omega_s = \int d\omega_0 \delta(\omega_s - \omega_0)$$

Then,

$$\begin{aligned} \sigma &= \pi \int d\omega_0 \int d\omega_s \frac{\omega_s^2}{c^3} d\Omega' [F(E_{\vec{q}} - \mu) - F(E_{\vec{p}} - \mu)] N(E_{\vec{p}} - E_{\vec{q}}) \\ &\quad \delta((E_{\vec{q}} - E_{\vec{p}}) - (\omega_0 - \omega_s)) \delta((\vec{k} - \vec{k}') - (\vec{q} - \vec{p})) \delta(\omega_s - \omega_0) \frac{V}{(2\pi)^3} \\ &= \int d\omega_0 d\Omega' \frac{\pi \omega_0^2}{c^3} [F(E_{\vec{q}} - \mu) - F(E_{\vec{p}} - \mu)] N(E_{\vec{p}} - E_{\vec{q}}) \\ &\quad \delta((E_{\vec{q}} - E_{\vec{p}}) - (\omega_0 - \omega_s)) \delta((\vec{k} - \vec{k}') - (\vec{q} - \vec{p})) \frac{V}{(2\pi)^3} \end{aligned}$$

Restoring the leading constants, we get the well known result for the Thompson scattering differential crosssection

$$\frac{d^2\sigma}{d\Omega d\omega_0} = \left[\frac{e^2}{m c^2} \right]^2 \hbar^2 c \frac{V}{2} \pi \frac{\omega_0}{\omega_s} |\hat{\epsilon}_0 \cdot \hat{\epsilon}_s|^2$$

$$[F(E_{\hat{q}} - \mu) - F(E_{\hat{p}} - \mu)] N(E_{\hat{p}} - E_{\hat{q}})$$

$$\delta((E_{\hat{q}} - E_{\hat{p}}) - (\omega_0 - \omega_s)) \delta((\vec{k} - \vec{k}') - (\vec{q} - \vec{p}))$$